Microtubular Fe/Mn-promoted CaO-Ca$_{12}$Al$_{14}$O$_{33}$ bi-functional material for H$_2$ production from sorption enhanced water gas shift

Chunxiao Zhang [a], Yingjie Li [a,*], Zirui He [b], Jianli Zhao [a], Dong Wang [c]

[a] *Shandong Engineering Laboratory for High-efficiency Energy Conservation and Energy Storage Technology & Equipment, School of Energy and Power Engineering, Shandong University, Jinan 250061, China*
[b] *Institute of Mechanics, Materials and Civil Engineering (iMMC), Materials & Process Engineering (IMAP), Université Catholique de Louvain, Place Sainte Barbe 2, B-1348 Louvain-la-Neuve, Belgium*
[c] *Brook Byers Institute for Sustainable Systems and School of Civil and Environmental Engineering, Georgia Institute of Technology, GA 30332, United States*

ARTICLE INFO

ABSTRACT

Herein, a hollow microtubular Fe/Mn-promoted CaO-Ca$_{12}$Al$_{14}$O$_{33}$ bi-functional material was prepared by the bio-template method and used for H$_2$ production from sorption enhanced water gas shift (SEWGS). The microtubular Fe/Mn-promoted CaO-Ca$_{12}$Al$_{14}$O$_{33}$ exhibits excellent CO$_2$ capture and H$_2$ production performance in SEWGS/regeneration cycles. The stable hollow microtubular structure improves available adsorption and catalytic sites in Fe/Mn-promoted CaO-Ca$_{12}$Al$_{14}$O$_{33}$ for CO$_2$ capture and H$_2$ production. Mn addition improves CO$_2$ affinity capacity of the microtubular material. The Fe-Mn interaction increases redox ability of Fe^{3+}/Fe$^{3+,2+}$, which promotes CO conversion. Moreover, the formed Ca$_2$Fe$_2$O$_5$ and Ca$_2$MnO$_4$ both increase oxygen vacancies to promote catalytic activity of the microtubular material for WGS and its CO$_2$ capture capacity. The CO conversions for the microtubular material with the Fe/Mn/Al/Ca molar ratio= 10/2/10/100 are 98.7% and 94.0% after 20 cycles under the mild and severe calcination conditions, respectively. The hollow microtubular bi-functional material shows good prospect for efficient H$_2$ production from SEWGS.

1. Introduction

Hydrogen is a promising energy carrier to produce, transport and store energy due to its high heating value, rich resources and environmental benefit [1,2]. At present, the majority of H$_2$ in the industrial applications comes from fossil fuels [3,4]. Water gas shift (WGS) reaction (as shown in Eq. (1)) is extensively used to reduce the CO concentration and upgrade the H$_2$ purity in various H$_2$ production processes, including steam methane reforming, steam reforming of glycerin, and steam gasification of biomass and coal, etc. [5]. Moreover, the WGS reaction is also used to convert CO in the by-product gases including coke oven gas and blast furnace gas from steel production to produce H$_2$ [6]. Consequently, the resource utilization of steelmaking off-gas is achieved.

$$CO + H_2O \rightarrow H_2 + CO_2 \tag{1}$$

There are limitations in the WGS reaction, including thermodynamic limitations at high temperature and slow kinetics at low temperature [7,8]. These restrictions can be weakened via sorption enhanced water gas shift (SEWGS) reaction conducted by in-situ removal of CO$_2$ in the WGS process [9,10]. The removal of CO$_2$ shifts the forward WGS reaction based on the Le Chatelier principle to produce more H$_2$ [11]. The SEWGS reaction can be operated at the mediate-temperature (200–400 °C) and the high-temperature (400–650 °C), depending on the working temperatures of various CO$_2$ sorbents [12–14]. MgO, Li-based sorbents and hydrotalcite-like sorbents can be employed as the mediate-temperature sorbents (200–400 °C) for SEWGS reaction. However, compared with those of the high-temperature sorbents (400–650 °C), the relatively lower CO$_2$ sorption capacities as well as the lower sorption and regeneration rates of the mediate-temperature sorbents limit their practical applications [15]. Calcium looping (CaL), i.e., the carbonation/calcination cycles of CaO-based sorbents (as shown in Eq. (2)), is a promising high-temperature CO$_2$ capture technology [16]. Although the regeneration of CaO at high calcination temperatures requires the high energy consumption, the advantages of using CaO sorbents for SEWGS are prominent, which include the relatively high CO$_2$ capture capacity and fast carbonation kinetics of CaO at 600–700 °C, as well as the large abundance of natural low-cost precursors [15,17]. Therefore, CaO

---

* Corresponding author.
E-mail address: liyj@sdu.edu.cn (Y. Li).

sorbents are appropriate for the high-temperature SEWGS process, as illustrated in Fig. 1 [18–20]. CO_2 generated from the WGS reaction reacts with CaO to form $CaCO_3$ and promote CO conversion (as shown in Eq. (3)) [21,22]. The regeneration of CaO is then performed under oxy-fuel combustion, and high-purity CO_2 is obtained for storage and utilization [23].

$$CO_2 + CaO \leftrightarrow CaCO_3 \tag{2}$$

$$CO + H_2O + CaO \rightarrow H_2 + CaCO_3 \tag{3}$$

The CO_2 capture capacity of CaO is crucial for H_2 production in the SEWGS process. However, CaO is prone to severe sintering after multiple CaL cycles, especially under the severe calcination condition at high temperature under high CO_2 concentration, which results in a rapid decline in the CO_2 capture capacity [24,25]. Therefore, the H_2 production performance in the SEWGS process using CaL also rapidly decreases with the number of cycles [26]. The additives with high Tammann-temperature such as MgO [27], TiO_2 [28], ZrO_2 [29] and Al_3O_2 [30], etc. have been used to mitigate the sintering of CaO. The incorporation of calcium aluminates (e.g. $Ca_{12}Al_{14}O_{33}$) formed by the reaction of CaO and Al_2O_3 in the preparation process has been reported to efficiently improve the cyclic stability of CaO in the multiple CaL cycles [31,32].

Moreover, the modification of the pore structure of CaO-based sorbent can also efficiently improve its CO_2 capture performance in CaL cycles [33,34]. Highly porous morphologies are beneficial to mitigate the contact and agglomeration of CaO particles after multiple CaL cycles [35]. Moreover, the large surface area and pore volume of the CaO-based sorbent promote the solid-gas reaction between CaO and CO_2 [36,37]. Various porous CaO-based sorbents with hollow spherical and tubular structures have been prepared for CO_2 capture in CaL cycles [38, 39]. The outer and inner surfaces of these hollow CaO-based sorbents are exposed for gas diffusion, promoting gas-solid contact between CO_2 and CaO. Moreover, the hollow structures provide sufficient void space, which can mitigate the effect of volumetric change of $CaO/CaCO_3$ during multiple CaL cycles [40]. Nanosized and microsized CaO sorbents with porous structures have been reported for CO_2 capture [41–43]. The applications of the porous hollow CaO-based materials in CaL processes in recent years are summarized in Table 1. In particular, biological materials with the unique hollow tubular morphology have been directly utilized as the bio-templates to prepare the microtubular CaO-based materials to avoid the complicated preparation of the template [44,45]. The applications of the hollow microtubular CaO-based materials for CO_2 capture and CaL heat storage have been investigated. However, the application for sorption enhanced H_2 production in SEWGS process has been rarely reported.

The use of catalysts to promote CO conversion is another effective approach for SEWGS [23]. In this regard, the combination of active catalysts with CO_2 sorbents to prepare the bi-functional materials is crucial [47–49]. Meng et al. [50] developed a bi-functional material for H_2 production in SEWGS process at 600 °C, which consisted of the CaO core and Al_2O_3-supported Ni catalyst shell. It was demonstrated that more than 97% CO was converted to H_2. Kim et al. [19] prepared the Ni nanoparticles with hollow CaO-based spheres stabilized by a thin layer of Al_2O_3 through an atomic layer deposition method, which showed

effective and stable H_2 production performance over several SEWGS/regeneration cycles. However, Ni is toxic and is found to catalyze the conversion of CO to CH_4 by the methanation reaction (as shown in Eq. (4)) [50]. CH_4 is an undesirable by-product in the WGS process, which will reduce the concentration of H_2. The mixtures of Fe_2O_3 and Cr_2O_3 are typically used as the high-temperature catalysts in the industrial WGS processes [51]. However, the chromium component is toxic and carcinogenic [52]. Therefore, it is necessary to develop the alternative chromium-free Fe-based catalyst for WGS reaction [53]. Fe/CaO material has been proposed for sorption enhanced H_2 production processes [54,55]. Zamboni et al. [56] reported that both the presence of the Fe_2O_3 phase and the formation of the $Ca_2Fe_2O_5$ phase between iron and calcium exhibited the positive catalytic effect on the WGS reaction. Furthermore, transition metal modification using Cu, Co, Ce, Ni and Mn, etc., has been investigated to promote the activity and thermal stability of Fe-based catalysts in the high-temperature WGS reaction [57–59]. However, the effect of Mn on the Fe/CaO bi-functional materials for SEWGS reaction has not been reported.

$$CO + 3H_2 \rightarrow CH_4 + H_2O \tag{4}$$

In this work, we aimed to fabricate a porous material with high CO_2 capture and active catalytic performance as well as high cyclic stability for promoting H_2 production in SEWGS. We proposed the novel application of hollow microtubular bi-functional materials in SEWGS process. A novel hollow microtubular Fe/Mn-promoted CaO-$Ca_{12}Al_{14}O_{33}$ was fabricated by the bio-template method, containing CaO sorbent, Fe-based catalyst, Mn promoter and $Ca_{12}Al_{14}O_{33}$ stabilizer. The CO_2 capture capacity and H_2 production performance in the SEWGS process using the hollow microtubular bi-functional materials were investigated. The microstructural evolution of the hollow microtubular bi-functional material in the SEWGS/regeneration cycles was determined. The effect of Mn addition on H_2 production performance and CO_2 capture using hollow microtubular Fe-promoted CaO-$Ca_{12}Al_{14}O_{33}$ in the cyclic SEWGS process was studied. This work is expected to achieve efficient and stable simultaneous H_2 production/CO_2 capture from SEWGS cycles.

2. Experimental

2.1. Raw materials

Absorbent paper as a representative of bio-template was used. Ca$(C_2H_3O_2)_2 \cdot H_2O$ (≥99.0 wt%, Shanghai Aladdin Industrial Co., Ltd., China), Al$(NO_3)_3 \cdot 9 H_2O$ (≥99.0 wt%, Sinopharm Chemical Reagent Co., Ltd., China), Fe$(NO_3)_3 \cdot 9 H_2O$ (≥99.9 wt%, Shanghai Aladdin Industrial Co., Ltd., China) and Mn$(C_2H_3O_2)_2 \cdot 4 H_2O$ (≥99.0 wt%, Shanghai Aladdin Industrial Co., Ltd., China) were used as calcium, aluminum, iron and manganese precursors, respectively. Moreover, Ni $(C_2H_3O_2)_2 \cdot 4 H_2O$ (≥99.0 wt%, Shanghai Macklin Biochemical Co., Ltd., China) was used as nickel precursor.

2.2. Preparation of hollow microtubular bi-functional materials

The synthesis schematic of the hollow microtubular Fe/Mn-promoted CaO-$Ca_{12}Al_{14}O_{33}$ is illustrated in Fig. 2. Firstly, 10 g of Ca $(C_2H_3O_2)_2 \cdot H_2O$ and calculated amounts of Al$(NO_3)_3 \cdot 9 H_2O$, Fe$(NO_3)_3) \cdot 9 H_2O$ and Mn$(C_2H_3O_2)_2 \cdot 4 H_2O$ were added to 100 mL of deionized water according to the specific molar ratio of Ca/Al/Fe/Mn to obtain a homogeneous mixed solution. Subsequently, a stack of absorbent paper was fully impregnated in the mixed solution for 24 h. Next, the wet paper was sequentially dried at 80 °C for 6 h and then combusted in air at 750 °C for 2 h to remove the template. Thus, the microtubular Fe/Mn-promoted CaO-$Ca_{12}Al_{14}O_{33}$ bi-functional materials were obtained. These materials were denoted as Fe$_x$Mn$_y$Al$_z$CaO-T, where x, y and z represent the molar ratios of Ca:Fe, Ca:Mn and Ca:Al are 100:x, 100:y and 100:z, respectively, and T means the template method. Moreover,
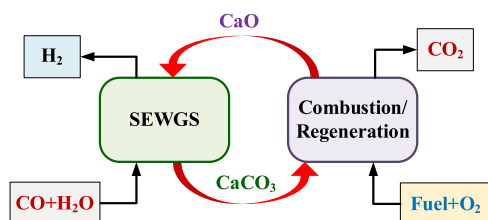

Fig. 1. Schematic diagram of H_2 production from SEWGS process using CaL.

Table 1

Composition and performance of CaO-based materials in different processes based on CaL.

| Material	Morphology	Preparation method	Application	Conditions (sorption/ regeneration)	Cycles	Sorption capacity (g-CO_2/g-sorbent)	Ref
Ni-CaO-$Ca_3Al_2O_6$	hollow nano-sphere	hydrothermal	SEWGS	650 °C, 20% CO_2, 1 bar /900 °C, 55% CO_2, 1 bar	1/30	0.54/0.43	[19]
CaO-$Ca_{12}Al_{14}O_{33}$	hollow micro-sphere	carbon sphere gel-template	CO_2 capture	750 °C, 40% CO_2, 1 bar /750 °C, 100% N_2, 1 bar	1/30	0.53/0.56	[39]
CaO	hollow micro-sphere	hydrothermal	CO_2 capture	650 °C, 15% CO_2, 1 bar /850 °C, 100% N_2, 1 bar	15	0.275	[33]
CaO-$Ca_9Al_6O_{18}$	hollow multishelled micro-sphere	hydrothermal	CO_2 capture	650 °C, 12% CO_2, 1 bar /900 °C, 100% CO_2, 1 bar	30	0.55	[40]
Ni-CaO-MgO	hollow micro-sphere	hydrothermal	sorption-enhanced steam reforming of glycerol	550 °C, 10% CO_2, 1 bar /800 °C, 100% N_2, 1 bar	1/10	0.49/0.37	[43]
CaO-$Ca_{12}Al_{14}O_{33}$	hollow micro-tube	bio-template	CO_2 capture	700 °C, 15% CO_2, 1 bar /920 °C, 70% CO_2, 1 bar	1/30	0.59/0.33	[38]
CaO-$Ca_{12}Al_{14}O_{33}$	hollow micro-tube	bio-template	CO_2 capture	700 °C, 20% CO_2, 1 bar /920 °C, 70% CO_2, 1 bar	1/30	0.61/0.41	[44]
CaO-$Ca_{12}Al_{14}O_{33}$	hollow micro-tube	bio-template	heat storage	850 °C, 100% CO_2, 13 bar /850 °C, 100% N_2, 1 bar	1/30	0.62/0.58	[46]
CeO_2-CaO-$Ca_{12}Al_{14}O_{33}$	hollow micro-tube	bio-template	heat storage	850 °C, 100% CO_2, 13 bar /850 °C, 100% N_2, 1 bar	1/30	0.73/0.72	[46]
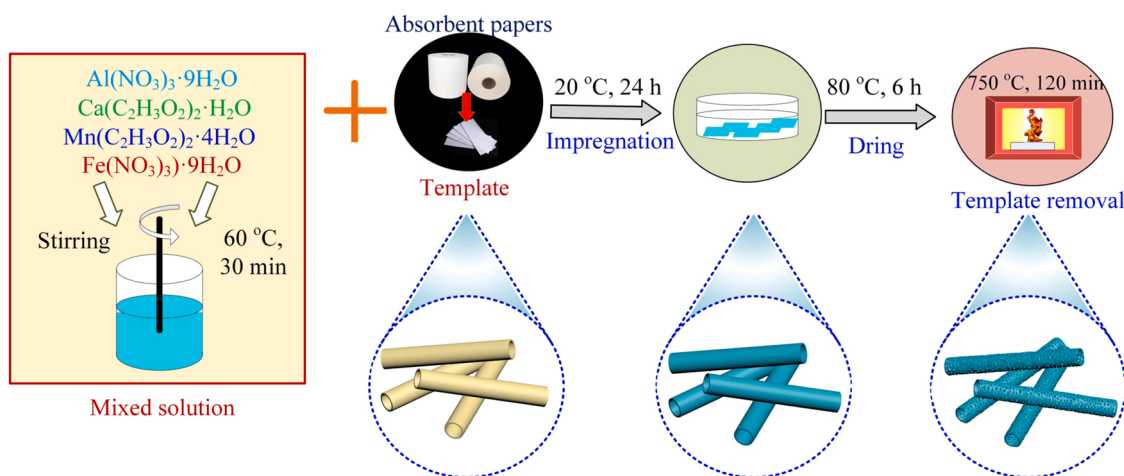
Fig. 2. Synthesis schematic of hollow microtubular bi-functional materials.

for the comparison, the microtubular monometallic Fe-promoted and Mn-promoted CaO-$Ca_{12}Al_{14}O_{33}$ were prepared according to the above-mentioned procedure, which were denoted as Fe_xAl_zCaO-T and Mn_yAl_zCaO-T, respectively. In addition, the bi-functional materials by the wet-mixing method were also synthesized by the similar procedure in the absence of the absorbent paper template, which were denoted as $Fe_xMn_yAl_zCaO$, Fe_xAl_zCaO and Mn_yAl_zCaO. Fe catalyst, Fe/Mn catalyst and Ni catalyst were also prepared by the template method as above-mentioned, which were denoted as Fe-T, Fe_xMn_y-T and Ni-T, respectively.

2.3. Cyclic CO_2 capture and SEWGS tests

The cyclic carbonation/calcination tests of the bi-functional materials (500 mg) were carried out in a dual fixed-bed reactors system. The experimental procedure was reported in the literature [38]. The carbonation was conducted in 15 vol% CO_2/30 vol% steam/N_2 at 600 °C for 20 min. The calcination was conducted under the severe condition with 70 vol% CO_2/N_2 at 920 °C and the mild condition with pure CO_2 at 850 °C for 10 min, respectively. The CO_2 capture capacity of the sample was calculated as follows:

$$C_N = \frac{m_{\text{carb, } N} - m_{\text{cal, } N}}{m_0} \qquad (5)$$

where N represents the number of the CaL cycles; C_N denotes the CO_2 capture capacity of the sample in the Nth CaL cycle, g/g; $m_{\text{carb, } N}$ and $m_{\text{cal, } N}$ indicate the sample mass after the Nth carbonation and calcination reactions, g, respectively; m_0 denotes the mass of the initial sample, g.

WGS and SEWGS reactions were performed in a vertical fixed-bed reactor, which is illustrated in Fig. 3. In a typical experiment, 1 g catalyst or bi-functional material was loaded on the quartz wool supported in a quartz tube. The flow rate of water was controlled by a syringe pump, and it was evaporated by a preheater kept at 130 °C to produce steam for the WGS and SEWGS reactions. The WGS and SEWGS reactions were performed at 400–700 °C. Prior to the test, the sample was heated from the room temperature to the desired temperature in Ar atmosphere at 10 °C/min. After reaching the stable temperature, a mixture of steam and CO swept by Ar at a total flow rate of 200 mL/min was introduced into the reactor to start the WGS/SEWGS reaction for 120 min. The concentration of CO was 4 vol%, and the corresponding volume ratios of steam to CO (S/C) were 1, 2, 4, 6 and 8, respectively. The product gas was cooled down by an ice-cooled bath where the condensable gas
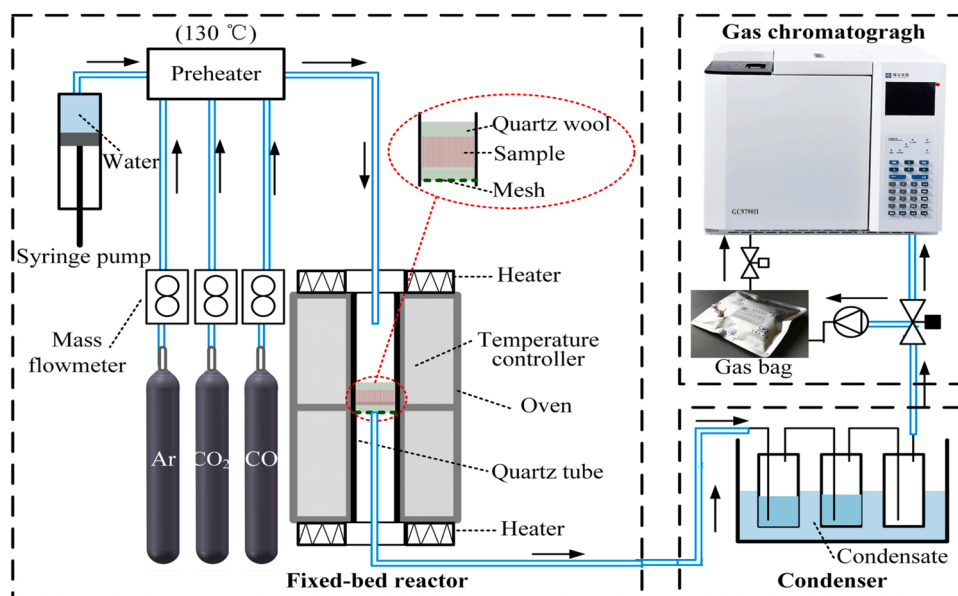
Fig. 3. Schematic diagram of a vertical fixed-bed SEWGS system.

(steam) was removed. Then the corresponding concentrations of CO, CO_2, H_2 and CH_4 in the product gas were measured on-line using a gas chromatograph (GC, 9790II, Fuli) equipped with a thermal conductivity detector (TCD). The data acquisition interval for GC was every 8 min. Moreover, the same groups of the experiments were repeated to collect the accumulated incondensable off-gas in the certain period by a gas bag. The average concentrations of CO, CO_2, H_2 and CH_4 in the product gas were also analyzed using GC. The cyclic SEWGS/regeneration tests were also performed in the vertical fixed-bed reactor. After a SEWGS reaction, the reactor was heated to the desired calcination temperature at 10 ℃/min for the regeneration of CaO. The regeneration was conducted under the severe calcination condition (920 ℃, 70 vol% CO_2/ 30 vol% Ar) and mild calcination condition (850 ℃, 100 vol% Ar) for 30 min, respectively. Then, a SEWGS/regeneration cycle was completed. The reactor was then cooled down to the desired SEWGS temperature. The SEWGS/regeneration reactions were repeated for 20 cycles.

The relative CO, CO_2, H_2 and CH_4 concentrations in the product gas were calculated by Eq. (6):

$$V_i = \frac{v_i}{v_{CO} + v_{CO_2} + v_{H_2} + v_{CH_4}} \tag{6}$$

where i denotes the components in the off-gas during WGS/SEWGS reaction, such as CO, CO_2, H_2, or CH_4; V_i represents the relative concentrations of CO, CO_2, H_2 and CH_4 in the product gas on Ar-free and dry basis, respectively, %; v_i denotes the volume fractions of CO, CO_2, H_2 and CH_4 in the product gas, respectively, vol%. The average CO conversion and H_2 yield were calculated as follows:

$$X_{CO} = \frac{F_{CO,\ in} - F_{CO,\ out}}{F_{CO,\ in}} \tag{7}$$

$$Y_{H_2} = \frac{F_{H_2,\ out}}{F_{CO,\ in}} \tag{8}$$

$$F_{CO,\ out} = \frac{F_{Ar}}{1 - (v_{CO} + v_{CO_2} + v_{H_2} + v_{CH_4})} \cdot v_{CO} \tag{9}$$

$$F_{H_2,\ out} = \frac{F_{Ar}}{1 - (v_{CO} + v_{CO_2} + v_{H_2} + v_{CH_4})} \cdot v_{H_2} \tag{10}$$

where X_{CO} represents the average CO conversion during the WGS/

SEWGS reaction, %; Y_{H2} is the average H_2 yield during the WGS/SEWGS reaction, %; $F_{CO,\ in}$ denotes the cumulative flow of CO in the gaseous input during the certain period, mL; $F_{CO,\ out}$ and $F_{H2,\ out}$ are the cumulative flows of CO and H_2 in the gaseous output, which were calculated based on the Ar balance, mL, respectively; and F_{Ar} is the cumulative flow of input Ar, mL.

2.4. Characterizations

The crystallinities and chemical compositions of the materials were examined by X-ray diffraction (XRD, D/max-rB). The Scherrer equation and Bragg equation were used to calculate the mean crystallite size and lattice parameter, respectively. The elemental compositions and valence states of the samples were detected by a Thermo ESCALAB 250XI X-ray photoelectron spec-troscopy (XPS). CO_2 temperature-programmed desorption (CO_2-TPD), O_2 temperature-programmed desorption (O_2-TPD) and H_2-temperature-programmed reduction (H_2-TPR) were performed using an AutoChem II 2920 Micromeritics to analyze the basicity, oxygen species and reducibility of the materials, respectively. Electron paramagnetic resonance (EPR) spectra was analyzed to determine the vacancies characteristics of the samples by a Bruker A300 spectrometer. The surface morphologies of the samples were characterized using a scanning electron microscope (SEM, JEOL JSM-7600 F). The elemental analysis on the surface of materials was performed using energy dispersive X-ray (EDX, Oxford INCA sight X). Transmission electron microscopy (TEM) images, high-resolution transmission electron microscopy (HRTEM) images, high angle annular dark field scanning transmission electron microscopy (HAADF-STEM) images and energy dispersive X-ray spectroscopic (EDS) element mappings were recorded in a FEI Tecnai G2 F20 operated at 200 kV.

3. Results and discussion

3.1. Morphology and phase composition of microtubular Fe/Mn-promoted/CaO-$Ca_{12}Al_{14}O_{33}$

Fig. 4(a) displays the XRD patterns of $Fe_{10}Mn_2Al_{10}$CaO-T, $Fe_{10}Al_{10}$-CaO-T and $Mn_{10}Al_{10}$CaO-T. The diffraction peaks corresponding to CaO and $Ca_{12}Al_{14}O_{33}$ are presented in the XRD patterns of these three bi-functional materials. The sharp diffraction peaks with high intensity confirm that CaO is the main product in the bi-functional materials.
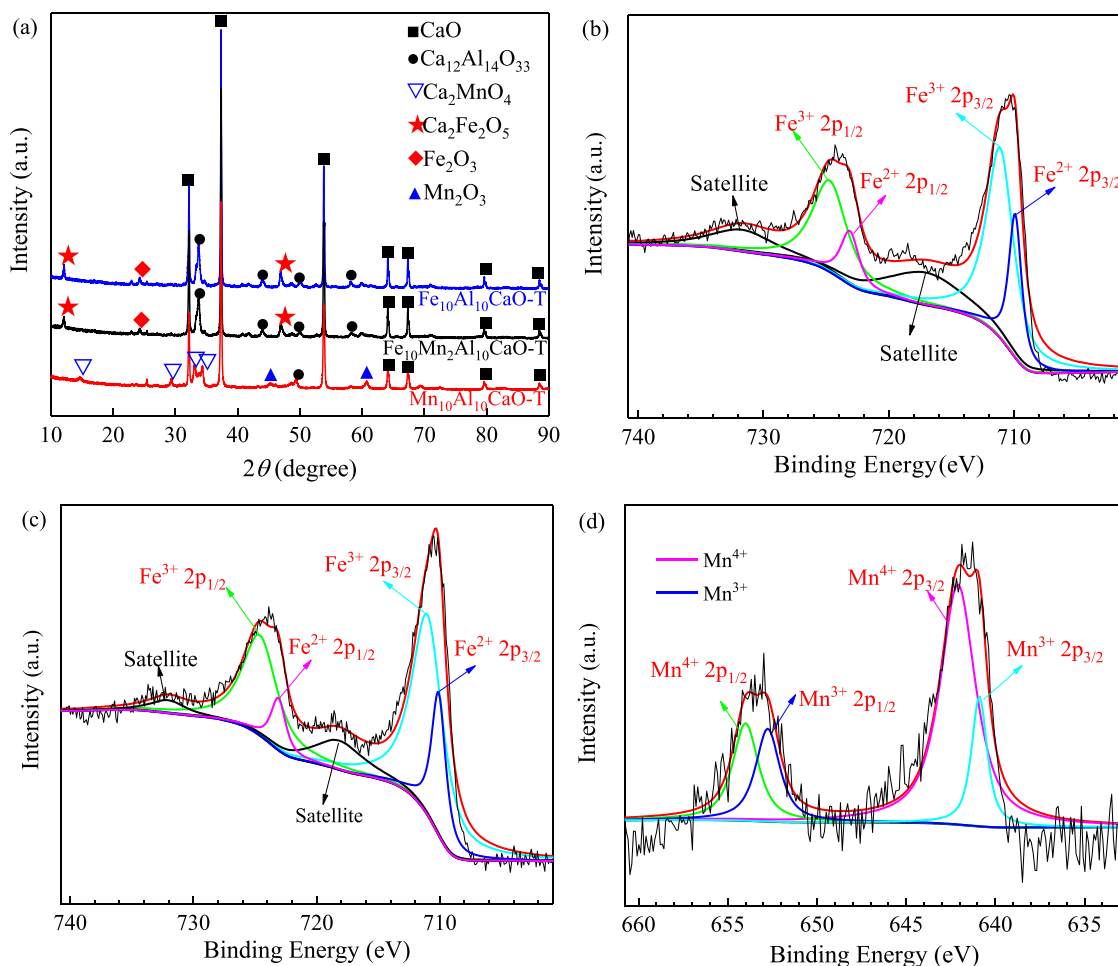
Fig. 4. XRD and XPS analysis of the bi-functional materials: (a) XRD patterns of $Fe_xMn_yAl_{10}CaO-T$, (b) XPS spectrum of Fe 2p of $Fe_{10}Al_{10}CaO-T$, (c) XPS spectrum of Fe 2p of $Fe_{10}Mn_2Al_{10}CaO-T$, (d) XPS spectrum of Mn 2p of $Fe_{10}Mn_2Al_{10}CaO-T$.

$Ca_{12}Al_{14}O_{33}$ is a solid solution formed by the interaction of Al_2O_3 and CaO after removing the template at 750 °C. The characteristic peaks of $Ca_2Fe_2O_5$ and Fe_2O_3 are presented in the XRD patterns of $Fe_{10}Mn_2Al_{10}CaO-T$ and $Fe_{10}Al_{10}CaO-T$, suggesting the formation of different iron phases. $Ca_2Fe_2O_5$ and Fe_2O_3 both exhibit high catalytic activities for the WGS reaction [56]. The peaks of Ca_2MnO_4 and Mn_2O_3 are found in the XRD pattern of $Mn_{10}Al_{10}CaO-T$. However, Mn is not detected in $Fe_{10}Mn_2Al_{10}CaO-T$ due to its low content. XPS analysis is used to analyze the valence states of the Fe and Mn in $Fe_{10}Mn_2Al_{10}CaO-T$. The Fe 2p spectrum of $Fe_{10}Al_{10}CaO-T$ possesses four dominant peaks and two satellite peaks, as illustrated in Fig. 4(b). The peaks located at binding energies of 709.9 eV for Fe $2p_{3/2}$ and 723.1 eV for Fe $2p_{1/2}$ are ascribed to Fe^{2+}, and the peaks at 711.1 eV for Fe $2p_{3/2}$ and 724.7 eV for Fe $2p_{1/2}$ correspond to Fe^{3+}, respectively [60,61]. The existence of Fe^{3+} confirms the compositions of $Ca_2Fe_2O_5$ and Fe_2O_3 in $Fe_{10}Al_{10}CaO-T$. However, there is no sign of a composition containing Fe^{2+} in the XRD patterns, probably because of the low loading of Fe^{2+}. $Fe_{10}Mn_2Al_{10}$-CaO-T also shows the characteristic peaks of Fe^{3+} and Fe^{2+}, as exhibited in Fig. 4(c). Compared with the monometallic $Fe_{10}Al_{10}CaO-T$, the Fe^{2+} and Fe^{3+} peaks in $Fe_{10}Mn_2Al_{10}CaO-T$ shift to the lower binding energies of 709.7 eV ($2p_{3/2}$) and 710.8 eV ($2p_{3/2}$), respectively. These changes suggest that the Fe-Mn interaction allows the electron transfer from Mn to Fe [62]. Furthermore, the Mn 2p peaks of $Fe_{10}Mn_2Al_{10}CaO-T$ indicate the existence of Mn^{4+}/Mn^{3+}, as shown in Fig. 4(d) [63,64]. This result indicates the formation of Ca_2MnO_4 and Mn_2O_3 in $Fe_{10}Mn_2Al_{10}CaO-T$, which are not observed in its XRD pattern. Therefore, $Ca_2Fe_2O_5$ and Fe_2O_3 phases are formed in $Fe_{10}Mn_2Al_{10}CaO-T$, and the doping of Mn

leads to the formation of Ca_2MnO_4 and Mn_2O_3. The average crystallite sizes and lattice parameters of $Fe_{10}Mn_2Al_{10}CaO-T$ and $Fe_{10}Al_{10}CaO-T$ calculated from the XRD results are listed in Table 2. The results indicate that the two samples have similar lattice parameters including d_{CaO} and $d_{Ca12Al14O33}$. However, the average crystallite sizes of CaO and $Ca_{12}Al_{14}O_{33}$ grains in $Fe_{10}Mn_2Al_{10}CaO-T$ are smaller than those in $Fe_{10}Al_{10}CaO-T$, respectively, indicating the structural promotion effect of Mn addition.

The SEM images of $Fe_{10}Mn_2Al_{10}CaO-T$ are exhibited in Fig. 5. $Fe_{10}Mn_2Al_{10}CaO-T$ exhibits a hollow tube-like morphology, as displayed in Fig. 5(a) and (b). $Fe_{10}Mn_2Al_{10}CaO-T$ possesses a highly porous tube wall, as illustrated in Fig. 5(c) and (d). The widths of the tubes vary from several to tens of μm, and the thickness of the tube wall is smaller than 1 μm. The high porosity of the hollow microtubular structure exposes more adsorption and catalytic sites and reduces the resistance of gas diffusion, resulting in better gas-solid contact in the SEWGS reaction. The porous hollow structure is also expected to provide sufficient void

Table 2
Average crystallite sizes and lattice parameters of the bi-functional materials.

Samples	D_{CaO}[a] (nm)	$D_{Ca12Al14O33}$[a] (nm)	d_{CaO}[b] (nm)	$d_{Ca12Al14O33}$[b] (nm)
$Fe_{10}Al_{10}CaO-T$	24.6	24.5	0.2892	0.2776
$Fe_{10}Mn_2Al_{10}CaO-T$	21.1	18.4	0.2893	0.2773

[a] Average crystallite size calculated by Scherrer equation.
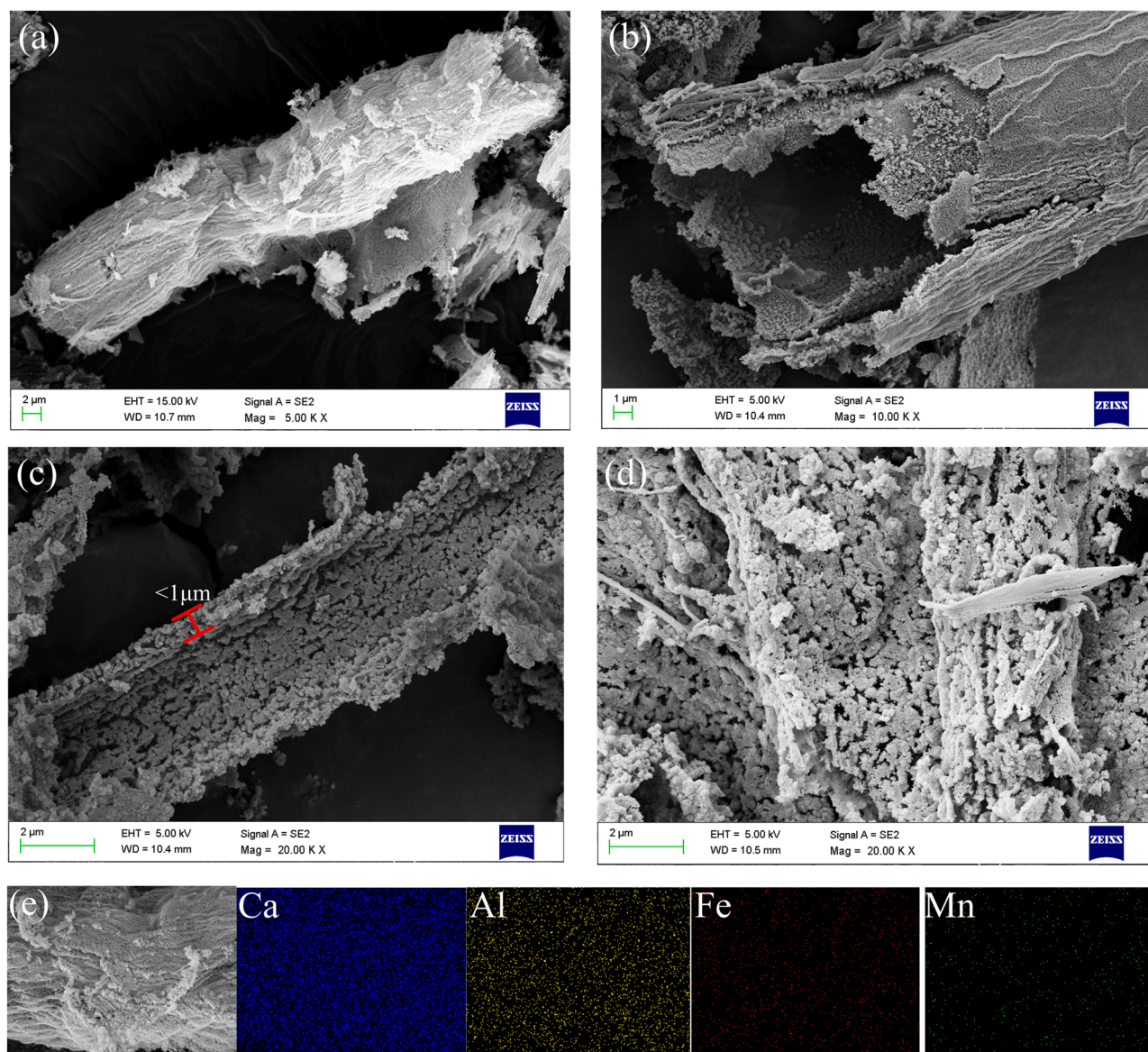[b] Lattice parameter calculated by Bragg equation.

Fig. 5. SEM images of $Fe_{10}Mn_2Al_{10}CaO$-T: (a) external view, (b) tube inlet, (c) sectional view, (d) tube surface, (e) SEM-EDX mapping.

space, which offsets the large volume changes of $CaO/CaCO_3$. The SEM-EDX mapping exhibits the uniform distributions of Ca, Al, Fe and Mn elements on the surface of $Fe_{10}Mn_2Al_{10}CaO$-T, as shown in Fig. 5(e).

The microstructure of Fe/Mn-promoted/CaO-$Ca_{12}Al_{14}O_{33}$ is further investigated on nanoscale, as shown in Fig. 6. TEM images and crystal size distribution of $Fe_{10}Al_{10}CaO$-T and $Fe_{10}Mn_2Al_{10}CaO$-T are demonstrated in Fig. 6(a) and (b), respectively. Compared with $Fe_{10}Al_{10}CaO$-T, $Fe_{10}Mn_2Al_{10}CaO$-T comprises of the smaller nanosized crystals with the average size of 16.2 nm. The enlarged HRTEM image of $Fe_{10}Mn_2Al_{10}$-CaO-T shows obvious lattice fringes, as exhibited in Fig. 6(c). The lattice fringes of 0.272, 0.320, 0.279 and 0.251 nm are attributed to the (1 1 1) lattice plane of CaO, the (3 2 1) lattice plane of $Ca_{12}Al_{14}O_{33}$, the (0 0 2) lattice plane of $Ca_2Fe_2O_5$ and the (1 1 0) lattice plane of Fe_2O_3, respectively [46,65,66]. The results are consistent with the XRD results. Moreover, the lattice fringes of 0.184 and 0.224 nm are attributed to the (2 2 0) lattice plane of Ca_2MnO_4 and the (4 1 1) lattice plane of Mn_2O_3, respectively [67,68]. The HAADF-STEM image and the EDS element mappings are shown in Fig. 6(d)-(i). The EDS mappings of Ca, Al, Fe and Mn elements possess almost the same distribution patterns, indicating the uniform distribution of Ca, Al, Fe and Mn components. This result indicates the formation of well-mixed sorbents, catalysts, stabilizers and

promoters on the nanoscale in the microtubular bi-functional material.

3.2. Cyclic CO_2 capture performance of microtubular Fe/Mn-promoted/CaO-$Ca_{12}Al_{14}O_{33}$

The oxy-fuel combustion is required for CO_2 enrichment in the calcination stage. Therefore, bi-functional materials need to be calcined under the severe condition (high CO_2 concentration and high temperature above 900 ℃). Fig. 7 exhibits C_N of the microtubular Fe-promoted CaO-$Ca_{12}Al_{14}O_{33}$ under the severe calcination condition over 20 CaL cycles. The CO_2 capture capacity of $Fe_{10}Al_zCaO$-T in the first cycle decreases as the Al content increases. This is because with increased Al addition, more CaO is consumed to form $Ca_{12}Al_{14}O_{33}$, thereby reducing the CaO content in the microtubular Fe-promoted CaO-$Ca_{12}Al_{14}O_{33}$. However, compared with that of $Fe_{10}Al_zCaO$-T ($z > 0$), CO_2 capture capacity of $Fe_{10}CaO$-T shows a more rapid drop with the number of cycles. This result indicates $Ca_{12}Al_{14}O_{33}$ as a stabilizer improves the sintering resistance of the bi-functional materials. As N increases from 1 to 20, C_N of $Fe_{10}CaO$-T, $Fe_{10}Al_5CaO$-T, $Fe_{10}Al_{10}CaO$-T and $Fe_{10}Al_{15}CaO$-T decrease by 72%, 35%, 19% and 15%, respectively. The high Al content is beneficial for the cyclic stability of the CO_2 capture capacity of
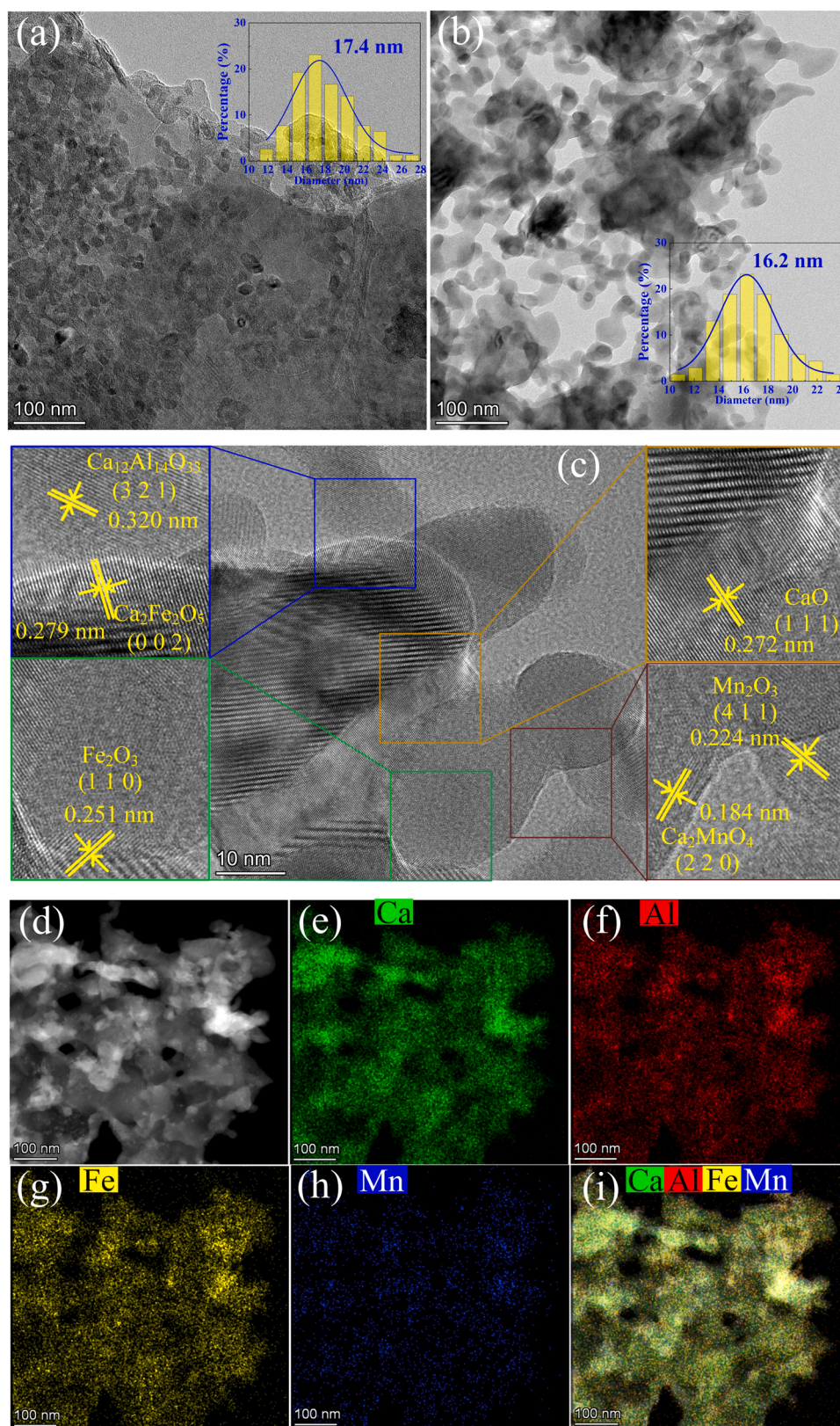
Fig. 6. TEM images of (a) $Fe_{10}Al_{10}CaO-T$ and (b) $Fe_{10}Mn_2Al_{10}CaO-T$, (c) HRTEM image of $Fe_{10}Mn_2Al_{10}CaO-T$, (d) HAADF-STEM image of $Fe_{10}Mn_2Al_{10}CaO-T$ and (e-i) the corresponding EDS mappings of $Fe_{10}Mn_2Al_{10}CaO-T$.
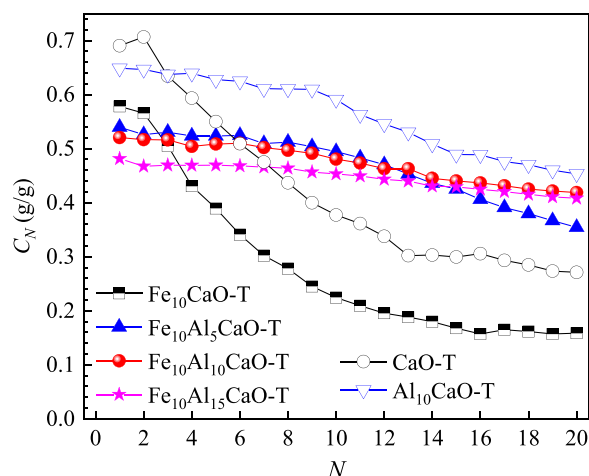
Fig. 7. CO_2 capture capacity of $Fe_{10}Al_zCaO$-T during 20 CaL cycles under severe calcination condition (carbonation: 15 vol% CO_2/30 vol% steam/N_2, 600 °C, 20 min; calcination: 70 vol% CO_2/N_2, 920 °C, 10 min).

the microtubular Fe-promoted CaO-$Ca_{12}Al_{14}O_{33}$. $Fe_{10}Al_{10}CaO$-T possesses the highest C_{20} among $Fe_{10}Al_zCaO$-T, which is 0.42 g/g. $Fe_{10}Al_{10}CaO$-T shows lower C_1 than $Al_{10}CaO$-T, because Fe addition reduces the CaO content. However, the decay of C_N in $Al_{10}CaO$-T over 20 cycles is higher than that in $Fe_{10}Al_{10}CaO$-T. $Fe_{10}Al_{10}CaO$-T exhibits the better cyclic stability than $Al_{10}CaO$-T, probably because the oxygen mobility characteristics of brownmillerite-structured $Ca_2Fe_2O_5$ is formed by doping Fe into CaO [69]. The oxygen vacancies can enhance the diffusion of CO_2 through the $CaCO_3$ product layer by providing O^{2-} ions to produce CO_3^{2-} [70]. Therefore, the cyclic stability of the microtubular bi-functional material in CaL cycles is improved.

The effect of Mn addition on the cyclic CO_2 capture by Fe-promoted CaO-$Ca_{12}Al_{14}O_{33}$ is investigated. C_N of the microtubular Fe/Mn-promoted CaO-$Ca_{12}Al_{14}O_{33}$ under the severe calcination condition is depicted in Fig. 8. $Fe_{10}Mn_yAl_{10}CaO$-T possesses the higher cyclic stability than $Fe_{10}Al_{10}CaO$-T under the severe calcination condition. However, the excess Mn reduces the CO_2 capture capacity of the microtubular bi-functional material, because Mn addition causes more consumption of the active CaO to form Ca_2MnO_4. Therefore, there is the optimum Ca/Mn ratio in the microtubular bi-functional material for cyclic CO_2 capture. $Fe_{10}Mn_2Al_{10}CaO$-T exhibits the highest C_{20} (0.43 g/g) among the different $Fe_{10}Mn_yAl_{10}CaO$-T under the severe calcination condition. The effect of Mn addition on the cyclic stability of
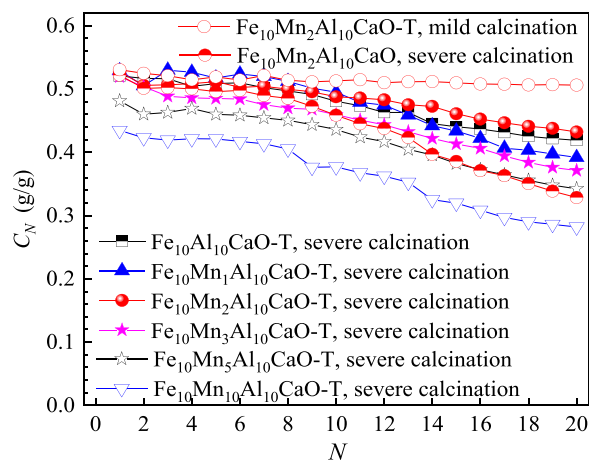
$Fe_{10}Mn_yAl_{10}CaO$-T is probably attributed to improved electron transfer due to Mn [71]. The layered-perovskite-structured Ca_2MnO_4 can provide more oxygen vacancies, which enhances CO_2 diffusion in the carbonation reaction [56]. In addition, C_N of $Fe_{10}Mn_2Al_{10}CaO$-T under the severe calcination (70% CO_2 and 920 °C) and mild calcination (pure N_2 and 850 °C) conditions are compared. $Fe_{10}Mn_2Al_{10}CaO$-T under the mild calcination exhibits the better cyclic stability in 20 CaL cycles than under the severe calcination. C_N of $Fe_{10}Mn_2Al_{10}CaO$-T under the mild calcination condition only drops by 5% with increasing N from 1 to 20. This result indicates that the bi-functional material under the severe calcination condition suffers from more serious sintering compared with the mild calcination condition. Moreover, $Fe_{10}Mn_2Al_{10}CaO$-T shows the significantly higher C_N than $Fe_{10}Mn_2Al_{10}CaO$. This result proves the superiority of the hollow microtubular structure for cyclic CO_2 capture.

3.3. SEWGS and WGS processes using Fe/Mn catalysts

Fig. 9 demonstrates the product profiles using Fe and Fe/Mn catalysts in WGS process. CH_4 is not detected in the product gas of the WGS reaction using Fe catalyst and Fe/Mn catalyst, indicating that the methanation reaction does not occur with Fe-based catalysts. Fe-T and $Fe_{10}Mn_2$-T both exhibit the stable performance within 120 min. Moreover, V_{H2} for $Fe_{10}Mn_2$-T is higher than that for Fe-T, and V_{CO} for $Fe_{10}Mn_2$-T is lower. This indicates Fe/Mn catalyst exhibits the higher catalytic effect on WGS reaction than Fe catalyst.

The comparison in the performance of the different catalysts in the WGS process is shown in Fig. 10. X_{CO} at 400–700 °C using the prepared catalysts is illustrated in Fig. 10 (a). The equilibrium conversion of CO in the WGS reaction based on the minimization of the Gibbs free energy is also presented. The equilibrium conversion of CO decreases with increasing the temperature, because the WGS reaction is exothermic. The catalytic activities of the different catalysts increase as T rises from 400 to 500 °C, which is attributed to the increased reaction rate at higher WGS temperature. X_{CO} for Ni-T and $Fe_{10}Mn_2$-T start to decay with further increasing the temperatures above 500 and 600 °C, respectively. This is due to the limitation of thermodynamic equilibrium. Fe catalyst exhibits the lower catalytic effect than Ni catalyst on WGS reaction. However, Mn addition significantly enhances the catalytic activity of Fe-based catalyst. X_{CO} follows the order of $Fe_{10}Mn_2$-T > Ni-T > Fe-T at 400–700 °C. $Fe_{10}Mn_2$-T shows the highest X_{CO} of 89.6% at 600 °C, which is close to the equilibrium value (92.8%). Fig. 10 (b) presents the H_2 yield using the different catalysts. Y_{H2} for $Fe_{10}Mn_2$-T and Fe-T are respectively equal to their X_{CO}, because only the WGS reaction occurs to produce H_2 and CO_2 without the by-product CH_4. Therefore, only X_{CO} is used and Y_{H2} is no longer used to illustrate the WGS and SEWGS performance of Fe/Mn-promoted/CaO-$Ca_{12}Al_{14}O_{33}$ in the following discussion. However, Y_{H2} for Ni-T is much lower than its X_{CO} due to the production of by-product CH_4 by the catalytic effect of Ni on the methanation reaction. Therefore, Fe/Mn catalyst is efficient for H_2 production in the WGS process.

Fig. 11 displays the SEWGS performance of $Fe_{10}Al_{10}CaO$-T and $Fe_{10}Mn_2Al_{10}CaO$-T in terms of the concentrations of H_2, CO and CO_2 in the product gas in the first cycle. The SEWGS reaction using the bi-functional materials proceeds in three stages related to the carbonation reactivity of CaO, i.e., pre-breakthrough, breakthrough and post-breakthrough stages [19]. The pre-breakthrough period in the SEWGS reaction is related to the fast surface reaction-controlled stage of carbonation reaction of CaO. Obviously, CO_2 volume fraction remains at a low level in the pre-breakthrough stage. The pre-breakthrough period achieves high CO conversion and high-purity H_2, so a long duration of this period is highly desirable. The durations of the pre-breakthrough stage for $Fe_{10}Al_{10}CaO$-T and $Fe_{10}Mn_2Al_{10}CaO$-T are 40 and 60 min, respectively. Moreover, V_{H2} in the pre-breakthrough stage for $Fe_{10}Mn_2Al_{10}CaO$-T in the first cycle is higher than that for $Fe_{10}Al_{10}CaO$-T. As the carbonation of CaO begins to enter the slow product layer diffusion-controlled stage, the concentration of CO_2 in the off-gas starts
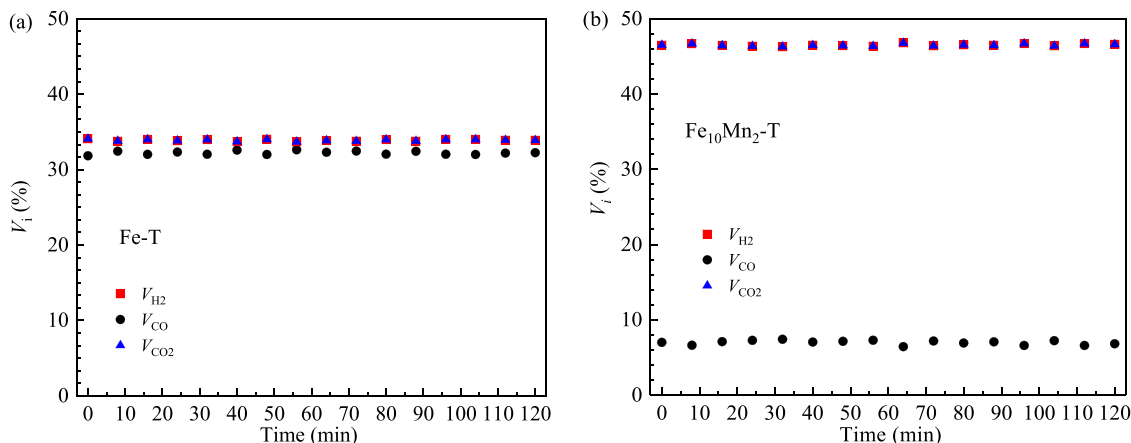

Fig. 8. CO_2 capture capacity of $Fe_{10}Mn_yAl_{10}CaO$-T during 20 CaL cycles (carbonation: 15 vol% CO_2/30 vol% steam/N_2, 600 °C, 20 min; calcination: 10 min).

Fig. 9. Typical WGS product profiles over Fe/Mn catalysts: (a) Fe-T, (b) $Fe_{10}Mn_2$-T (600 °C, 4% CO, S/C = 6).
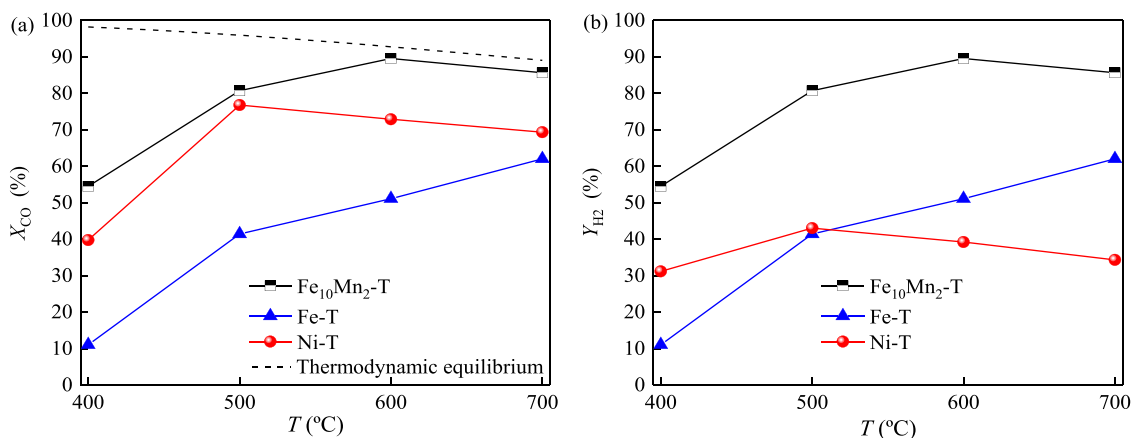

Fig. 10. CO conversion and H_2 yield for Fe/Mn catalysts in WGS reaction: (a) CO conversion, (b) H_2 yield (4% CO, S/C = 6).
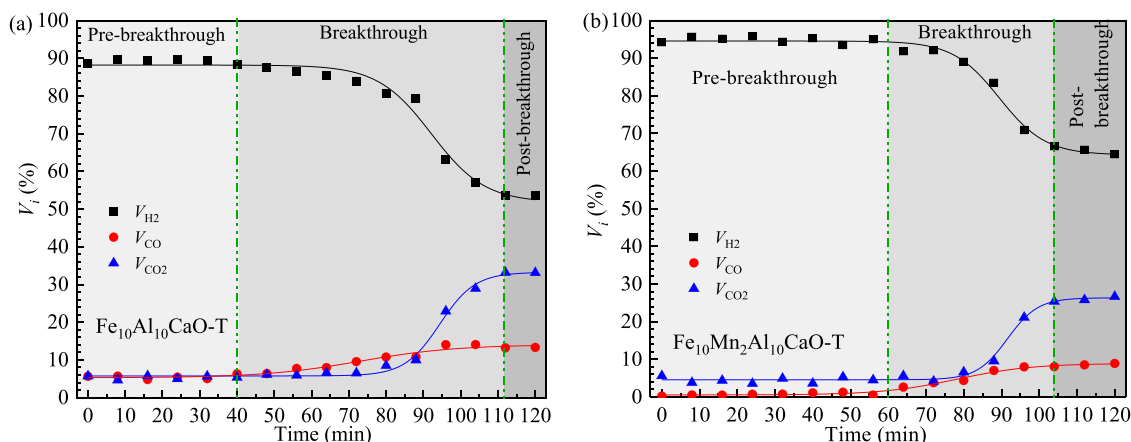

Fig. 11. Typical SEWGS product profiles in the first cycle using bi-functional materials: (a) $Fe_{10}Al_{10}CaO$-T, (b) $Fe_{10}Mn_2Al_{10}CaO$-T (600 °C, 4% CO, S/C = 6).

to increase, indicating that the breakthrough stage of the SEWGS reaction occurs. During this stage, the H_2 purity and CO conversion decrease rapidly as the carbonation rate decays. When the carbonation reaction of the material is in the slow diffusion-controlled stage, the SEWGS reaction shifts to the post-breakthrough stage.

3.4. SEWGS performance of microtubular Fe-promoted/CaO-$Ca_{12}Al_{14}O_{33}$ for H_2 production

Fig. 12 illustrates the effects of the reaction temperature, the volume ratio of S/C and the molar ratio of Ca/Fe on the SEWGS performance of the microtubular Fe-promoted CaO-$Ca_{12}Al_{14}O_{33}$ in the first cycle. The operation time for the SEWGS process is limited to 60 min. As the reaction temperature increases from 400 to 600 °C, X_{CO} increases significantly from 15.7% to 94.6% at the volume ratio of S/C = 6, as presented
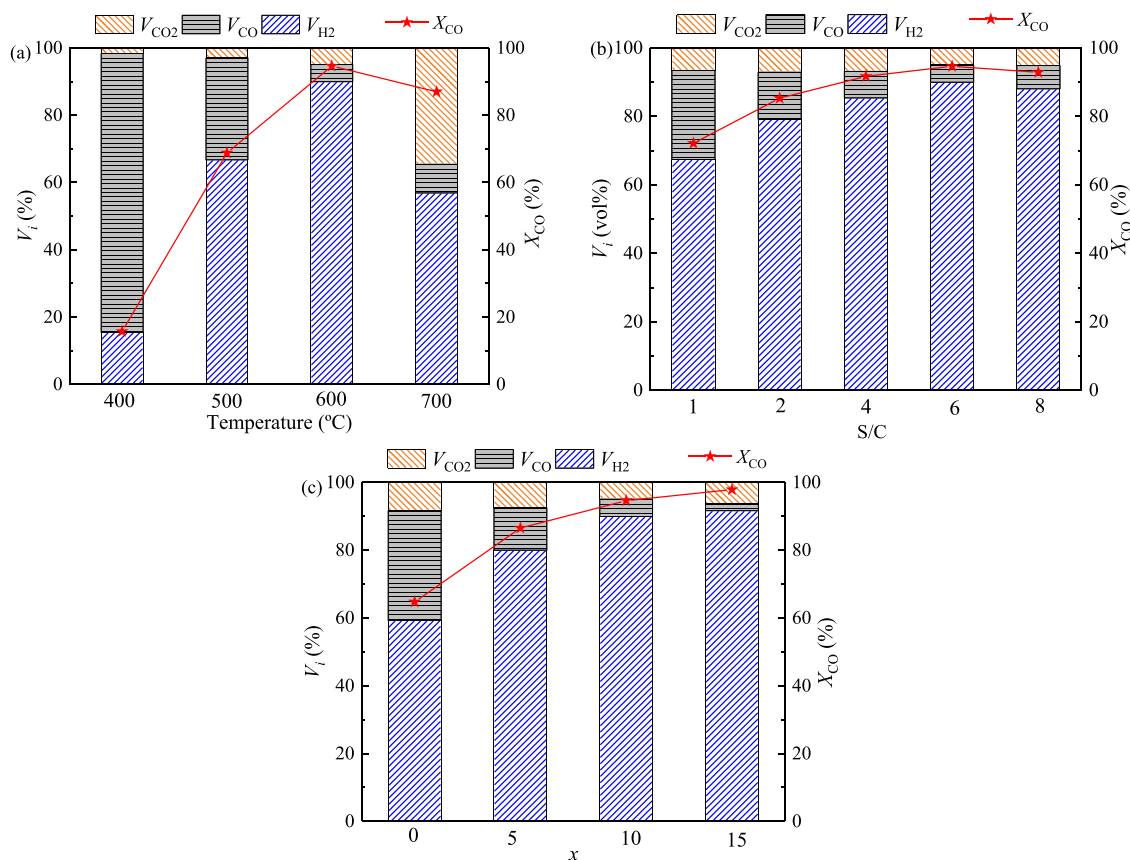
Fig. 12. Effects of temperature, volume ratio of S/C and molar ratio of Ca/Fe on SEWGS performance of microtubular Fe-promoted $CaO-Ca_{12}Al_{14}O_{33}$ in the first cycle: (a) temperature ($Fe_{10}Al_{10}CaO-T$, 4% CO, S/C = 6), (b) volume ratio of S/C ($Fe_{10}Al_{10}CaO-T$, 600 °C, 4% CO); (c) molar ratio of Ca/Fe (600 °C, 4% CO, S/C = 6).

in Fig. 12 (a). This is because the carbonation reaction rate is accelerated with increasing the temperature, leading to a high V_{H2} of 90.0% at 600 °C. However, X_{CO} for $Fe_{10}Al_{10}CaO-T$ drops rapidly as the temperature further increases to 700 °C, due to the thermodynamic limitation of the WGS reaction. Moreover, the exothermic carbonation reaction is also inhibited at higher temperature, which decreases the CO_2 capture capacity of the bi-functional material and results in reduced CO conversion. X_{CO} and V_{H2} decrease to 87.0% and 56.9% at 700 °C, respectively. Furthermore, X_{CO} at 600 °C is improved with increasing the volume ratio S/C from 1 to 6, while it decreases as S/C further increases from 6 to 8, as exhibited in Fig. 12 (b). This is probably because the high volume fraction of steam in the SEWGS process inhibits the catalytic activity. In general, the optimum reaction temperature and volume ratio of S/C for SEWGS are 600 °C and 6, respectively, which are employed in the following research. The Ca/Fe molar ratio also shows an important effect on the SEWGS performance of $Fe_xAl_{10}CaO-T$, as shown in Fig. 12 (c). Higher X_{CO} is achieved as x increases from 0 to 15. However, V_{CO2} for $Fe_{15}Al_{10}CaO-T$ is higher than that for $Fe_{10}Al_{10}CaO-T$. The higher Fe loading in $Fe_{15}Al_{10}CaO-T$ leads to the formation of the more catalytic sites, but it decreases the active CaO content, which is not beneficial for CO_2 capture. The molar ratio of Ca/Fe = 100:10 is suitable for $Fe_x-Al_{10}CaO-T$ to simultaneously achieve high X_{CO} and low V_{CO2}. The higher CO conversion and CO_2 capture capacity lead to better SEWGS performance using $Fe_{10}Al_{10}CaO-T$. Therefore, $Fe_{10}Al_{10}CaO-T$ possesses the highest H_2 production performance in the SEWGS process among the various Fe-promoted $CaO-Ca_{12}Al_{14}O_{33}$.

Fig. 13 displays the SEWGS performance of $Fe_{10}Al_{10}CaO-T$ in 20 SEWGS/regeneration cycles under the severe calcination condition. The operation time for the SEWGS reaction is limited to 60 min X_{CO} and V_{H2} in the syngas for these materials decrease with the number of cycles. Meanwhile, V_{CO} and V_{CO2} for the bi-functional materials increase with

the number of cycles. After 20 cycles, X_{CO} for $Fe_{10}Al_{10}CaO$ and $Fe_{10}CaO-T$ drop by 18.9% and 22.4%, respectively. $Fe_{10}Al_{10}CaO-T$ exhibits the good SEWGS performance and the cyclic stability, achieving a high X_{CO} of 88.3% and V_{H2} of 81.0% after 20 cycles. X_{CO} for $Fe_{10}Al_{10}CaO-T$ decreases by only 6.7% over 20 cycles. This result indicates the high cyclic stability of $Fe_{10}Al_{10}CaO-T$ is attributed to the synergetic effects of the hollow microtubular morphology and the support of $Ca_{12}Al_{14}O_{33}$.

3.5. SEWGS performance of microtubular Fe/Mn-promoted CaO-$Ca_{12}Al_{14}O_{33}$ for H_2 production

The SEWGS performance of $Fe_{10}Mn_yAl_{10}CaO-T$ in the first cycle under the severe calcination condition is presented in Fig. 14. Compared with $Fe_{10}Al_{10}CaO-T$, $Mn_yAl_{10}CaO-T$ exhibits the lower CO conversion. For instance, X_{CO} for $Mn_2Al_{10}CaO-T$ and $Mn_{10}Al_{10}CaO-T$ are 90.4% and 93.2%, respectively. This indicates that the SEWGS performance of Mn-promoted $CaO-Ca_{12}Al_{14}O_{33}$ is lower than that of Fe-promoted $CaO-Ca_{12}Al_{14}O_{33}$. The bimetallic $Fe_{10}Mn_yAl_{10}CaO-T$ possesses higher SEWGS performance than the monometallic $Mn_yAl_{10}CaO-T$ and $Fe_xAl_{10}CaO-T$. $Fe_{10}Mn_2Al_{10}CaO-T$ exhibits the highest X_{CO} of 99.3%, highest V_{H2} of 95.4% and lowest V_{CO2} of 4.0%. This result indicates the remarkable synergetic effect of Fe/Mn in the SEWGS process. However, excessive Mn addition in $Fe_{10}Mn_yAl_{10}CaO-T$ reduces X_{CO} and V_{H2}. When y is above 2, X_{CO} of $Fe_{10}Mn_yAl_{10}CaO-T$ begins to decrease, and V_{CO2} in the syngas increases. Therefore, $Fe_{10}Mn_2Al_{10}CaO-T$ is optimal among the various microtubular Fe/Mn-promoted $CaO-Ca_{12}Al_{14}O_{33}$ bi-functional materials to achieve the highest SEWGS performance.

The effect of the volume ratio of S/C on the SEWGS performance of $Fe_{10}Mn_2Al_{10}CaO-T$ is illustrated in Fig. 15. An increase in X_{CO} for $Fe_{10}Mn_2Al_{10}CaO-T$ is found with increasing the volume ratio of S/C from 1 to 6, while it decreases as the volume ratio of S/C further

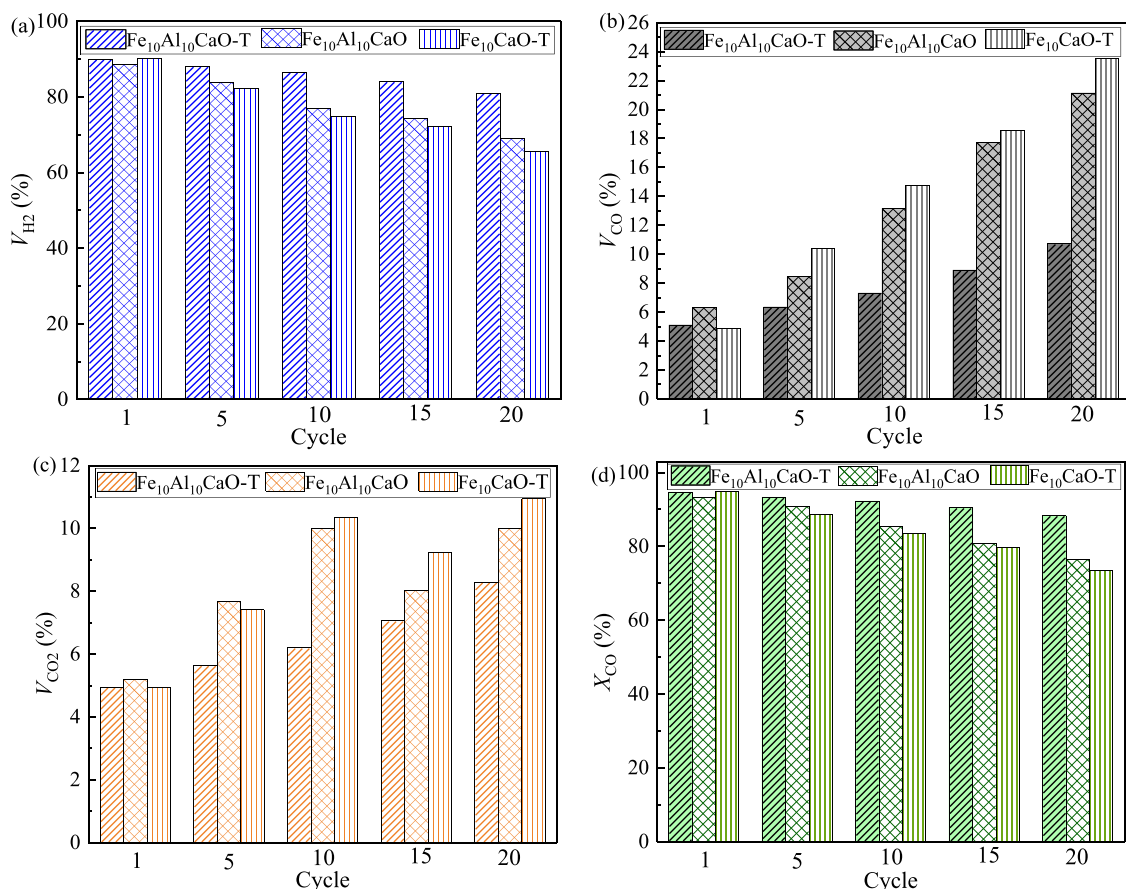**Fig. 13.** SEWGS performance of Fe-promoted CaO-$Ca_{12}Al_{14}O_{33}$ during 20 cycles under severe calcination condition: (a) V_{H2}, (b) V_{CO}, (c) V_{CO2}, (d) X_{CO} (600 °C, 4% CO, S/C = 6).

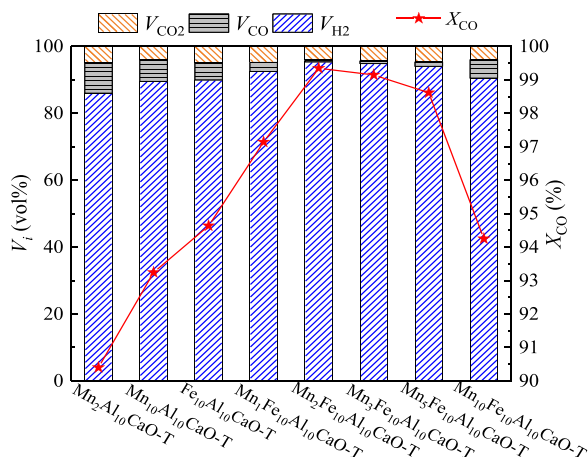**Fig. 14.** Effect of Mn addition on SEWGS performance of microtubular Fe-promoted CaO-$Ca_{12}Al_{14}O_{33}$ bi-functional materials in the first cycle (600 °C, 4% CO, S/C = 6).
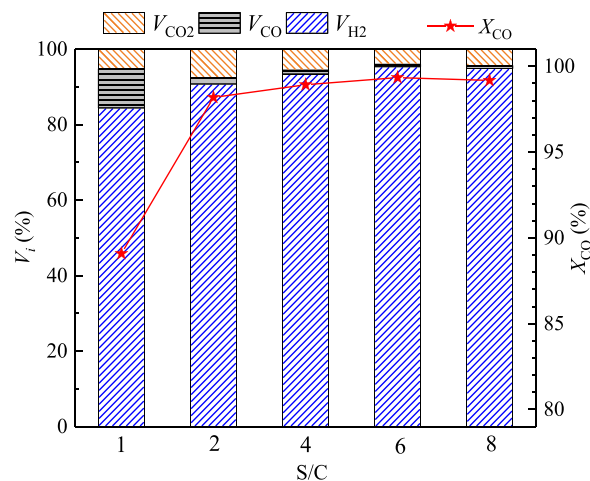

Fig. 15. Effect of volume ratio of S/C on SEWGS performance of $Fe_{10}Mn_2Al_{10}CaO$-T in the first cycle (600 °C, 4% CO).

increases to 8. The optimal volume ratio of S/C for $Fe_{10}Mn_2Al_{10}CaO$-T is 6, which is consistent with that for $Fe_{10}Al_{10}CaO$-T. However, it is illustrated that $Fe_{10}Mn_2Al_{10}CaO$-T shows high SEWGS activity even at a relatively low volume ratio of S/C, which differs from $Fe_{10}Al_{10}CaO$-T as shown in Fig. 12 (b). For instance, V_{H2} for $Fe_{10}Al_{10}CaO$-T at the volume ratios of S/C = 2 and 4 are 79.2% and 85.4%, while these for $Fe_{10}Mn_2Al_{10}CaO$-T are 90.8% and 93.4%, respectively. X_{CO} for $Fe_{10}Mn_2Al_{10}$-CaO-T at the volume ratio of S/C = 2 is as high as 98.2%, which is 15.1% higher than that for $Fe_{10}Al_{10}CaO$-T. Therefore, a low volume ratio of S/C

(e.g., 2) is appropriate for the SEWGS process using $Fe_{10}Mn_2Al_{10}CaO$-T.

Fig. 16 presents the CO conversion and product gas composition in 20 SEWGS/regeneration cycles under the severe calcination condition using $Fe_{10}Mn_2Al_{10}CaO$-T. The SEWGS performance of $Fe_{10}Mn_2Al_{10}CaO$-T decreases slightly with the number of cycles. $Fe_{10}Mn_2Al_{10}CaO$-T exhibits a high X_{CO} of 94.0% after 20 cycles, which is 16% and 23% higher than those for $Fe_{10}Mn_2Al_{10}CaO$ and $Fe_{10}Mn_2CaO$-T, respectively. Compared with $Fe_{10}Al_{10}CaO$-T (as exhibited in Fig. 13), $Fe_{10}Mn_2Al_{10}$-CaO-T possesses the higher and more stable cyclic SEWGS performance.
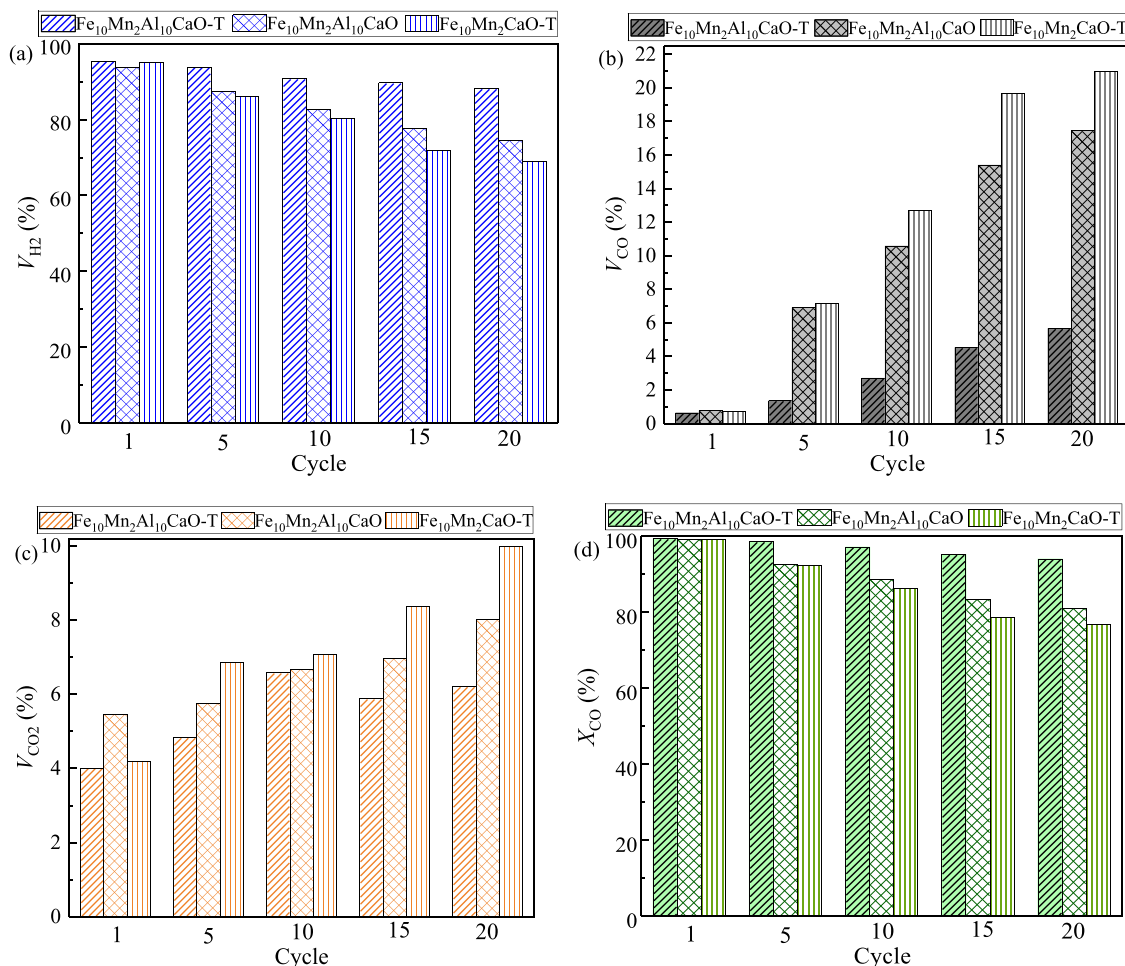
Fig. 16. SEWGS performance of microtubular Fe/Mn-promoted CaO-Ca$_{12}$Al$_{14}$O$_{33}$ bi-functional materials during 20 cycles under severe calcination condition: (a) V_{H2}, (b) V_{CO}, (c) V_{CO2}, (d) X_{CO} (600 °C, 4% CO, S/C = 6).

V_{H2}, V_{CO} and V_{CO2} for Fe$_{10}$Mn$_2$Al$_{10}$CaO-T after 20 SEWGS/regeneration cycles under the severe calcination condition are 88.1%, 5.7% and 6.2%, respectively. This is attributed to the addition of Mn, which simultaneously enhances the CO$_2$ capture performance and the catalytic activity for WGS reaction. The SEWGS performance of Fe$_{10}$Mn$_2$Al$_{10}$CaO-T during 20 cycles under the mild calcination condition is also determined, as
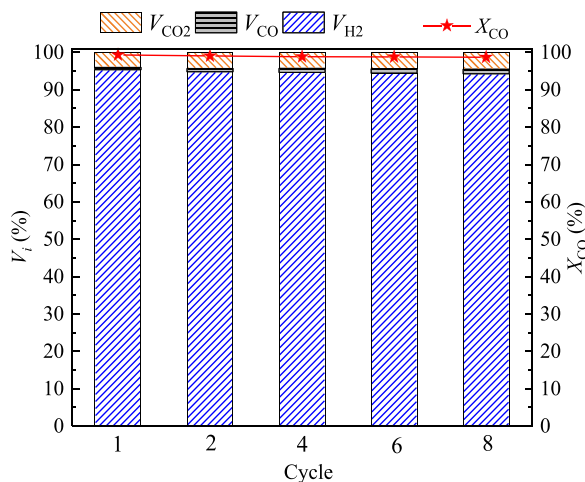
shown in Fig. 17. It is demonstrated that Fe$_{10}$Mn$_2$Al$_{10}$CaO-T exhibits much stable cyclic SEWGS performance under the mild calcination condition. V_{H2} and X_{CO} for Fe$_{10}$Mn$_2$Al$_{10}$CaO-T after 20 SEWGS/regeneration cycles under the mild calcination condition are as high as 94.3% and 98.7%, respectively. Moreover, the enhanced H$_2$ production performance using Fe$_{10}$Mn$_2$Al$_{10}$CaO-T in this work and other bi-functional materials reported in the literature are compared, as listed in Table 3. Although a realistic comparison with the results from the references is difficult because the reaction conditions using the different bi-functional materials are quite different, it can be concluded that the microtubular Fe/Mn-promoted CaO-Ca$_{12}$Al$_{14}$O$_{33}$ exhibits the excellent performance in terms of CO$_2$ capture capacity and enhanced H$_2$ production activity in the cycles.

3.6. Physicochemical properties of microtubular Fe/Mn-promoted CaO-Ca$_{12}$Al$_{14}$O$_{33}$

The CO$_2$-TPD patterns of Fe$_{10}$Mn$_2$Al$_{10}$CaO-T and Fe$_{10}$Al$_{10}$CaO-T are shown in Fig. 18. Fe$_{10}$Al$_{10}$CaO-T exhibits a strong CO$_2$ desorption peak at 657 °C, which is attributed to the strong basic sites of CaO. It is found that the main CO$_2$ desorption peak of Fe$_{10}$Mn$_2$Al$_{10}$CaO-T shifts toward a higher temperature at 676 °C and the peak intensity is improved. This result indicates Fe$_{10}$Mn$_2$Al$_{10}$CaO-T possesses the higher basicity than Fe$_{10}$Al$_{10}$CaO-T due to the Mn addition. It has been reported that the enhancement of the basicity can improve the affinity of acidic CO$_2$ to promote the CO$_2$ capture capacity of the CaO-based material [73]. Therefore, Fe$_{10}$Mn$_2$Al$_{10}$CaO-T exhibits the higher CO$_2$ capture capacity

Fig. 17. SEWGS performance of Fe$_{10}$Mn$_2$Al$_{10}$CaO-T during 20 cycles under mild calcination condition (600 °C, 4% CO, S/C = 6).

Table 3

Comparison in H_2 production performance using $Fe_{10}Mn_2Al_{10}CaO-T$ and different bi-functional materials reported in references during sorption enhanced steam reforming processes for H_2 production.

Bi-functional material	Reagent	Reaction conditions (sorption enhanced H_2 production; regeneration)	Cycles	Conversion of reagent (%)	H_2 yield (%)	Sorption capacity (g-CO_2/g-sorbent)	Ref
Ni/CeO_2-ZrO_2-CaO	Acetic acid	550 °C, S/C= 4; 750 °C, 100% Ar	1/15	~94/~88	~80/~50	0.30/0.27	[72]
Ni-CaO-MgO	Glycerol	550 °C, S/C= 4; 800 °C, 100% N_2	1/10	99.5/98.2	92.6/89.9	0.49/0.37	[43]
Ni-Ce/CaO-$Ca_3Al_2O_6$	Glycerol	550 °C, S/C= 3; 800 °C, 100% Ar	1/10	~95/-	~84/~83	~0.41/~0.35	[49]
Ni-CaO-fly ash	Glycerol	550 °C, S/C= 3; 800 °C, 100% N_2	1/20	–	~90/~90	0.58/0.45	[48]
Ni-CaO-$Ca_3Al_2O_6$	CO	600 °C, S/C= 2; 800 °C, 100% N_2	1/10	61.3/-	–	0.53/~0.51	[19]
$Fe_{10}Mn_2Al_{10}CaO-T$	CO	600 °C, S/C= 6; 920 °C, 70% CO_2/Ar	1/20	99.3/94.0	99.3/94.0	0.53/0.43	This work
$Fe_{10}Mn_2Al_{10}CaO-T$	CO	600 °C, S/C= 6; 850 °C, 100% Ar	1/20	99.3/98.7	99.3/98.7	0.53/0.51	This work
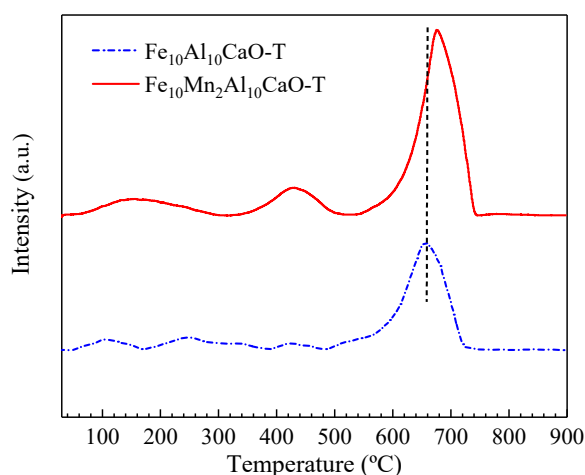
Fig. 18. CO_2-TPD patterns of $Fe_xMn_yAl_{10}CaO-T$.

than $Fe_{10}Al_{10}CaO-T$. As a result, H_2 production from SEWGS using the microtubular Fe-promoted CaO-$Ca_{12}Al_{14}O_{33}$ bi-functional material is also enhanced by the addition of Mn.

The H_2-TPR analysis results of $Fe_{10}Mn_2Al_{10}CaO-T$, $Fe_{10}Al_{10}CaO-T$ and $Mn_2Al_{10}CaO-T$ are illustrated in Fig. 19. There are three reduction peaks in the TPR curve of $Fe_{10}Al_{10}CaO-T$. Among them, the first peak located at 578 °C and the second at 712 °C are attributed to the consecutive reduction of Fe_2O_3 to Fe_3O_4 to FeO, respectively, which are also observed in $Fe_{10}Mn_2Al_{10}CaO-T$. It has been proven that the
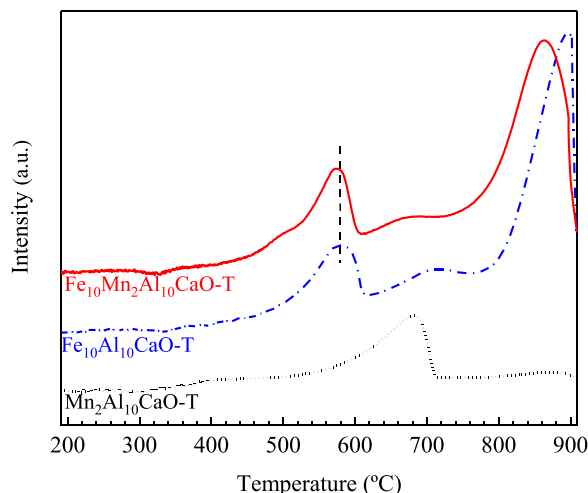

Fig. 19. H_2-TPR patterns of $Fe_xMn_yAl_{10}CaO-T$.

formation of Fe_3O_4 is responsible for the excellent catalytic performance during the WGS reaction, while the over-reduction of Fe_2O_3 to FeO or Fe^0 decreases the CO conversion [74]. At the SEWGS temperature of 600 °C, the reduction of Fe_2O_3 to Fe_3O_4 occurs, while the reduction to FeO or Fe^0 is limited for $Fe_{10}Al_{10}CaO-T$ and $Fe_{10}Mn_2Al_{10}CaO-T$, indicating the excellent catalytic activity in SEWGS. It is found that the two characteristic reduction peaks shift to the lower temperature for $Fe_{10}Mn_2Al_{10}CaO-T$, compared with those for $Fe_{10}Al_{10}CaO-T$. Moreover, a shoulder peak located at 492 °C is present for $Fe_{10}Mn_2Al_{10}CaO-T$ due to the interaction between Fe and Mn. These results indicate that the catalytic activity of $Fe_{10}Mn_2Al_{10}CaO-T$ based on the redox cycle of $Fe^{3+}/Fe^{3+,\ 2+}$ is improved by Mn addition. A strong reduction peak located at 800–900 °C is observed in the cases of $Fe_{10}Al_{10}CaO-T$ and $Fe_{10}Mn_2Al_{10}CaO-T$ due to the reduction of the $Ca_2Fe_2O_5$ phase into Fe^0. It has been proven that $Ca_2Fe_2O_5$ exhibits catalytic activity for the WGS reaction, which depends on the presence of oxygen vacancies in the $Ca_2Fe_2O_5$ structure [56]. The reduction temperature of $Ca_2Fe_2O_5$ is much higher than the operating temperature of the SEWGS reaction. This result illustrates that the $Ca_2Fe_2O_5$ phase keeps stable for $Fe_{10}Mn_2Al_{10}CaO-T$ and $Fe_{10}Al_{10}CaO-T$ in the SEWGS process. There is a reduction peak at above 600 °C in the H_2-TPR pattern of $Mn_2Al_{10}CaO-T$, which is related to the reduction of the Mn-containing phase. However, this peak is absent for $Fe_{10}Mn_2Al_{10}CaO-T$ due to the overlap with the reduction peak of the iron phase. Therefore, the WGS catalytic sites in $Fe_{10}Mn_2Al_{10}CaO-T$ are contributed by the $Ca_2Fe_2O_5$ phase and the redox cycle of $Fe^{3+}/Fe^{3+,\ 2+}$. Mn addition improves the reducibility of Fe_2O_3 to Fe_3O_4, thereby promoting CO conversion to produce H_2 in the SEWGS process.

The O 1 s XPS spectra of $Fe_{10}Mn_2Al_{10}CaO-T$ and $Fe_{10}Al_{10}CaO-T$ are illustrated in Fig. 20 (a). The O 1 s XPS spectra of the two samples are deconvoluted into three peaks located at 532.1, 531.3 and 529.2 eV, which correspond to the surface adsorbed water species (O1), surface chemisorbed oxygen (O2) and lattice oxygen (O3), respectively [75,76]. The concentration of surface chemisorbed oxygen species is related to the surface oxygen vacancy [77]. Fig. 20 (b) demonstrates the concentrations of different oxygen species for $Fe_{10}Mn_2Al_{10}CaO-T$ and $Fe_{10}Al_{10}CaO-T$. The results indicate that surface chemisorbed oxygen (O2) is the dominant oxygen specie in the two samples. Moreover, O2 in the oxygen species of $Fe_{10}Mn_2Al_{10}CaO-T$ and $Fe_{10}Al_{10}CaO-T$ are 69.8% and 68.9%, respectively. $Fe_{10}Mn_2Al_{10}CaO-T$ exhibits higher O2 concentration than $Fe_{10}Al_{10}CaO-T$, indicating the better oxygen mobility due to Mn addition.

The O_2-TPD analyses of $Fe_{10}Mn_2Al_{10}CaO-T$ and $Fe_{10}Al_{10}CaO-T$ are conducted to further investigate the mobility of the surface oxygen species. According to the literature [77,78], the desorption capacities of oxygen species follow the order of O_2 (ads) > O_2^- (ads) > O^- (ads) > O^{2-} (latt), where O_2 (ads) represents the physical adsorption of O_2, O_2^- (ads) and O^- (ads) are the chemical adsorbed oxygen, and O^{2-} (latt) refers to lattice oxygen. $Fe_{10}Mn_2Al_{10}CaO-T$ and $Fe_{10}Al_{10}CaO-T$ show the similar desorption curves, as shown in Fig. 21. The weak peaks below 200 °C
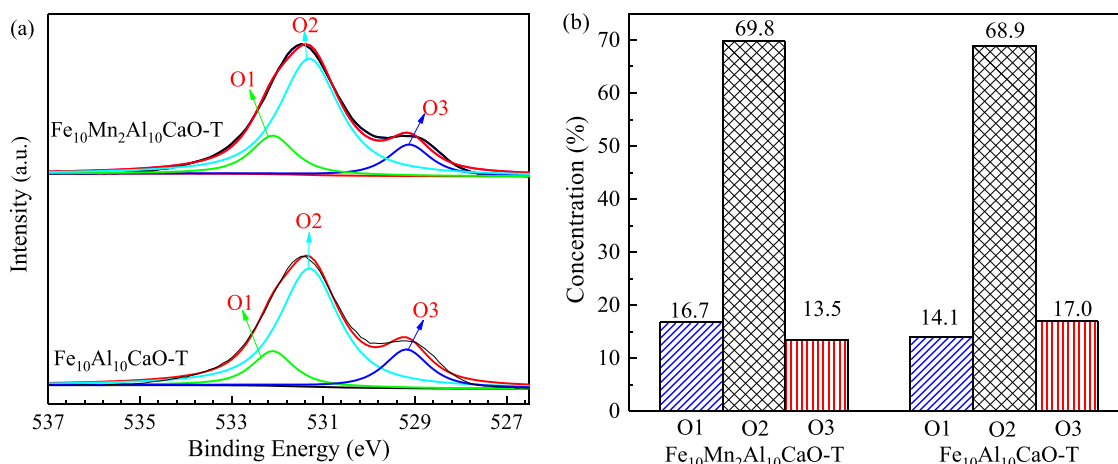
Fig. 20. XPS analyses of O 1 s of $Fe_{10}Mn_2Al_{10}CaO$-T and $Fe_{10}Al_{10}CaO$-T: (a) O 1 s XPS spectra, (b) concentrations of different oxygen species.
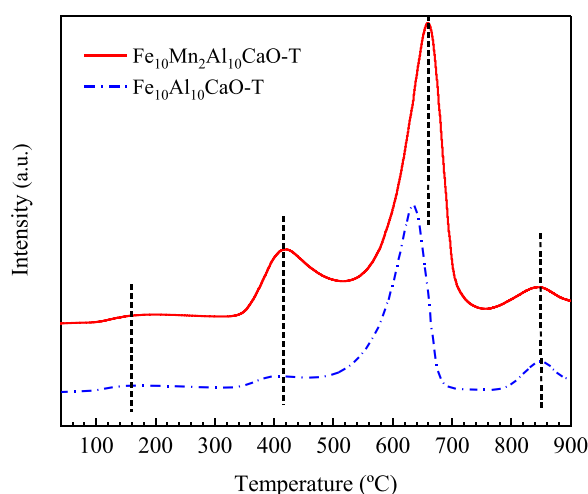
Fig. 21. O_2-TPD patterns of $Fe_{10}Mn_2Al_{10}CaO$-T and $Fe_{10}Al_{10}CaO$-T.

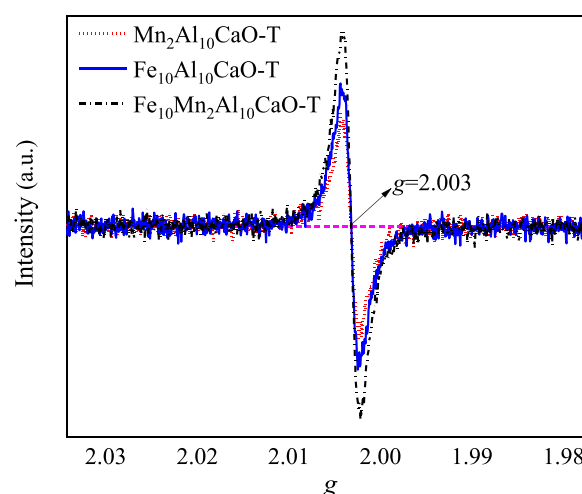**Fig. 22.** EPR spectra of $Fe_xMn_yAl_{10}CaO$-T.

and above 700 °C are attributed to the desorption of O_2 and lattice oxygen, respectively. $Fe_{10}Mn_2Al_{10}CaO$-T exhibits two main desorption peaks at 414 and 657 °C, which are associated with surface chemisorbed oxygen species (O_2 and O^-). Moreover, the areas of the two peaks for $Fe_{10}Mn_2Al_{10}CaO$-T are larger compared with $Fe_{10}Al_{10}CaO$-T, indicating the enhanced mobility of surface chemisorbed oxygen species due to Mn addition. This result also agrees with the result of XPS analysis.

The EPR analyses of $Fe_{10}Mn_2Al_{10}CaO$-T, $Fe_{10}Al_{10}CaO$-T and $Mn_2Al_{10}CaO$-T are presented in Fig. 22. The signal at $g = 2.003$ is observed in the EPR spectra of all three microtubular materials, which is related to the formation of the oxygen vacancies [79,80]. However, the intensity of the signal at $g = 2.003$ in the different materials varies, in the order of $Fe_{10}Mn_2Al_{10}CaO$-T > $Fe_{10}Al_{10}CaO$-T > $Mn_2Al_{10}CaO$-T. $Fe_{10}Mn_2Al_{10}CaO$-T exhibits the highest concentration of oxygen vacancy among these three materials. The results demonstrate that Mn addition increases the oxygen vacancies of the microtubular bi-functional materials. Increased oxygen vacancies can reduce the diffusion resistance of O^{2-}, thus facilitating the catalytic activity of $Ca_2Fe_2O_5$ in the WGS reaction. Moreover, the diffusion of O^{2-} on the surface and bulk of the microtubular bi-functional material is favorable for the formation of intermediate CO_3^{2-}, which is beneficial for CO_2 absorption by CaO. The improvement of oxygen vacancies contributes to the excellent SEWGS performance of $Fe_{10}Mn_2Al_{10}CaO$-T.

3.7. Microstructural evolution of microtubular Fe/Mn-promoted CaO-$Ca_{12}Al_{14}O_{33}$ in cycles

The SEM images of $Fe_{10}Mn_2Al_{10}CaO$-T and $Fe_{10}Al_{10}CaO$-T after 20 SEWGS/regeneration cycles are exhibited in Fig. 23. $Fe_{10}Al_{10}CaO$-T and $Fe_{10}Mn_2Al_{10}CaO$-T maintain the hollow microtubular structure in the cycles, reflecting the stability of the unique structure prepared by bio-template method. Fig. 24 exhibits the morphologies of different Fe/Mn-promoted CaO-$Ca_{12}Al_{14}O_{33}$ bi-functional materials fabricated by the bio-template and the wet-mixing methods after 20 cycles. It is observed that $Fe_{10}Mn_2Al_{10}CaO$ suffers from the severe sintering experienced 20 cycles, which results in the obvious agglomeration of CaO grains. However, $Fe_{10}Mn_2Al_{10}CaO$-T exhibits more porous surface and possesses smaller CaO grains than $Fe_{10}Mn_2Al_{10}CaO$ after 20 cycles. This is because the hollow microtubular structure can mitigate the influence of volumetric change in CaO/$CaCO_3$ during the cycles, thereby restricting grain growth and agglomeration. Therefore, the hollow microtubular $Fe_{10}Mn_2Al_{10}CaO$-T possesses the high sintering resistance, which promotes the CO_2 capture and SEWGS performance as well as the cyclic stability.

3.8. Reaction mechanism over microtubular Fe/Mn-promoted CaO-$Ca_{12}Al_{14}O_{33}$ in SEWGS process

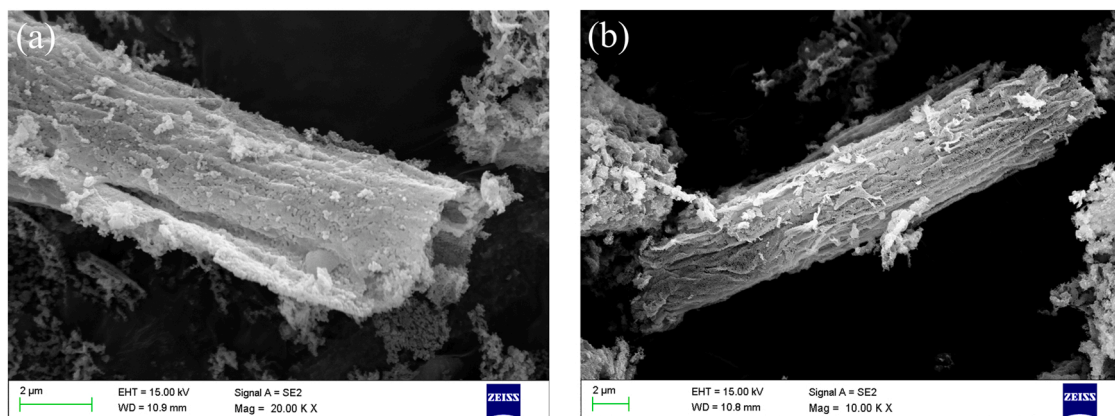The excellent H_2 production performance over the microtubular Fe/

Fig. 23. SEM images of $Fe_{10}Mn_2Al_{10}CaO-T$ (a) and $Fe_{10}Al_{10}CaO-T$ (b) after 20 SEWGS/regeneration cycles.
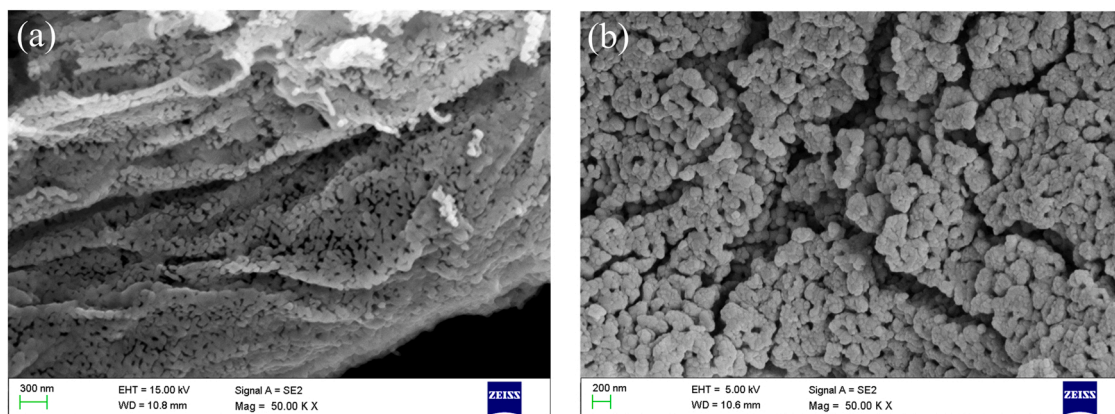
Fig. 24. High-magnification SEM images of $Fe_{10}Mn_2Al_{10}CaO-T$ (a) and $Fe_{10}Mn_2Al_{10}CaO$ (b) after 20 SEWGS/regeneration cycles.

Mn-promoted CaO-$Ca_{12}Al_{14}O_{33}$ in the SEWGS process is attributed to the synergetic effects of the porous hollow structure and the efficient activity of Fe/Mn catalyst for WGS reaction, as shown in Fig. 25. The porous hollow microtubular structure of $Fe_{10}Mn_2Al_{10}CaO-T$ exposes the outer and inner surfaces, increasing the available CO_2 adsorption and catalytic sites and reducing the resistance of gas diffusion, which is beneficial to the WGS and carbonation reactions. The activity of Fe-based catalyst in the microtubular Fe/Mn-promoted CaO-$Ca_{12}Al_{14}O_{33}$ for WGS is significantly improved by Mn addition due to the improved redox ability and the increased oxygen vacancies. The interaction of Fe-Mn allows the electron transfer from Mn to Fe, facilitating the $Fe^{3+}/Fe^{3+, 2+}$ redox ability to catalyze the WGS reaction. The layered-

perovskite-structured Ca_2MnO_4 contributes to more oxygen vacancies, which is favorable for the diffusion of O^{2-} in the WGS reaction to produce H_2. Moreover, the CO_2 affinity of the bi-functional material is promoted by Mn addition due to the improved basicity. This is beneficial to the in-situ CO_2 capture in the SEWGS process, thereby promoting H_2 production. The porous microtubular structure remains stable due to the support of $Ca_{12}Al_{14}O_{33}$. Therefore, the microtubular Fe/Mn-promoted CaO-$Ca_{12}Al_{14}O_{33}$ exhibits the excellent H_2 production performance and high cyclic stability during the SEGWS/regeneration cycles.

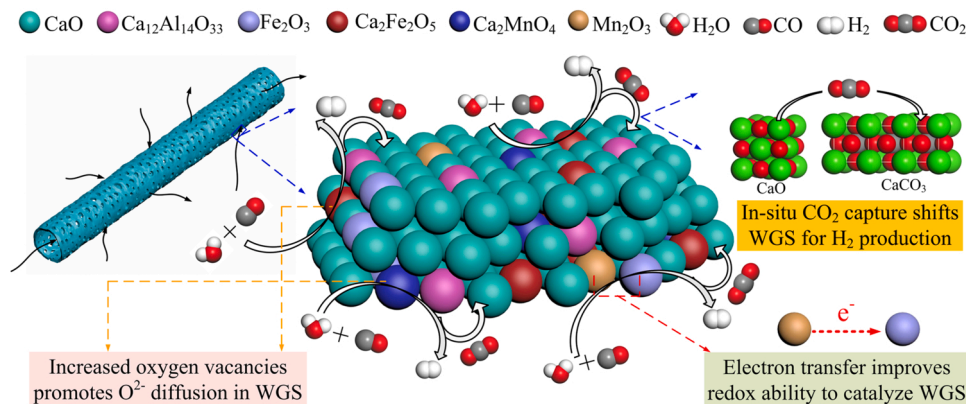**Fig. 25.** Mechanism diagram of microtubular Fe/Mn-promoted CaO-$Ca_{12}Al_{14}O_{33}$ in SEWGS process.

4. Conclusions

A hollow microtubular Fe/Mn-promoted CaO-$Ca_{12}Al_{14}O_{33}$ was fabricated by the bio-template method and evaluated for H_2 production in SEWGS/regeneration cycles. The experiments were carried out under the optimized SEWGS condition at 600 °C with the S/C volume ratio of 6 and under the severe calcination condition. The hollow microtubular structure exposes more available catalytic sites and adsorption sites for the WGS and carbonation reactions, respectively. The hollow microtubular structure of Fe/Mn-promoted CaO-$Ca_{12}Al_{14}O_{33}$ remains stable as a result of the support of $Ca_{12}Al_{14}O_{33}$, resulting in excellent cyclic stability during the repeated SEWGS/regeneration cycles. The synergistic effect of Fe/Mn in the microtubular Fe/Mn-promoted CaO-$Ca_{12}Al_{14}O_{33}$ promotes SEWGS for H_2 production. The interaction of Fe-Mn in the microtubular bi-functional material facilitates the $Fe^{3+}/Fe^{3+,\ 2+}$ redox ability to improve the WGS reaction. Mn addition increases the basicity of the microtubular bi-functional material, improving the affinity for CO_2. Moreover, the concentration of oxygen vacancies is increased by adding Fe and Mn to form $Ca_2Fe_2O_5$ and Ca_2MnO_4, which is beneficial to the WGS reaction and the CO_2 capture. The microtubular Fe/Mn-promoted CaO-$Ca_{12}Al_{14}O_{33}$ exhibits excellent SEWGS performance and very high cyclic stability in the SEWGS/regeneration cycles, which is attributed to the synergetic effects of the porous hollow microtubular structure and the addition of Fe/Mn. At the optimal Fe/Mn/Al/Ca molar ratio of 10/2/10/100, the CO conversion, H_2 concentration and CO_2 concentration in the first cycle using the microtubular bi-functional material are 99.3%, 95.4% and 4.0%, respectively. In addition, CO conversions retain 98.7% and 94.0% after 20 cycles under the mild and severe calcination conditions, respectively. Overall, the microtubular Fe/Mn-promoted CaO-$Ca_{12}Al_{14}O_{33}$ seems promising for application in H_2 production via SEWGS/regeneration cycles.

CRediT authorship contribution statement

Chunxiao Zhang: Data curation, Investigation, Visualization, Writing − original draft. **Yingjie Li:** Conceptualization, Methodology, Funding acquisition, Supervision, Writing − review & editing. **Zirui He:** Investigation. **Jianli Zhao:** Validation. **Dong Wang:** Investigation.

Declaration of Competing Interest

The authors declare that they have no known competing financial interests or personal relationships that could have appeared to influence the work reported in this paper.

Acknowledgments

References

[1] S.Z. Baykara, Hydrogen: A brief overview on its sources, production and environmental impact, Int J. Hydrog. Energy 43 (2018) 10605–10614.

[2] S. Dutta, A review on production, storage of hydrogen and its utilization as an energy resource, J. Ind. Eng. Chem. 20 (2014) 1148–1156.

[3] Z. Sun, H. Liu, H. Bai, S. Yu, C.K. Russell, L. Zeng, Z. Sun, The crucial role of deoxygenation in syngas refinement and carbon dioxide utilization during chemical looping-based biomass gasification, Chem. Eng. J. 428 (2022), 132068.

[4] M. Ji, J. Wang, Review and comparison of various hydrogen production methods based on costs and life cycle impact assessment indicators, Int J. Hydrog. Energy 46 (2021) 38612–38635.

[5] S.R.J. Byron, M. Loganathan, M.S. Shantha, A review of the water gas shift reaction kinetics, Int J. Chem. React. Eng. 8 (2010) 11–44.

[6] I. Dincer, C. Acar, Review and evaluation of hydrogen production methods for better sustainability, Int J. Hydrog. Energy 40 (2015) 11094–11111.

[7] E. Baraj, K. Ciahotny, T. Hlincik, The water gas shift reaction: Catalysts and reaction mechanism, Fuel 288 (2021), 119817.

[8] D. Lee, M.S. Lee, J.Y. Lee, S. Kim, H. Eom, D.J. Moon, K. Lee, The review of Cr-free Fe-based catalysts for high-temperature water-gas shift reactions, Catal. Today 210 (2013) 2–9.

[9] D. Li, Y. Cai, C. Chen, X. Lin, L. Jiang, Magnesium-aluminum mixed metal oxide supported copper nanoparticles as catalysts for water-gas shift reaction, Fuel 184 (2016) 382–389.

[10] G. Ji, J.G. Yao, P.T. Clough, J.C.D. Da Costa, E.J. Anthony, P.S. Fennell, W. Wang, M. Zhao, Enhanced hydrogen production from thermochemical processes, Energy Environ. Sci. 11 (2018) 2647–2672.

[11] A. Wright, V. White, J. Hufton, E.V. Selow, P. Hinderink, Reduction in the cost of pre-combustion CO_2 capture through advancements in sorption-enhanced water-gas-shift, Energy Procedia 1 (2009) 707–714.

[12] C.H. Lee, S. Kim, H.J. Yoon, C.W. Yoon, K.B. Lee, Water gas shift and sorption-enhanced water gas shift reactions using hydrothermally synthesized novel Cu-Mg-Al hydrotalcite-based catalysts for hydrogen production, Renew. Sust. Energy Rev. 145 (2021), 111064.

[13] J. Boon, P.D. Cobden, H.A.J. van Dijk, C. Hoogland, E.R. van Selow, M. van Sint Annaland, Isotherm model for high-temperature, high-pressure adsorption of and on K-promoted hydrotalcite, Chem. Eng. J. 248 (2014) 406–414.

[14] L.A. Živković, A. Pohar, B. Likozar, N.M. Nikačević, Kinetics and reactor modeling for CaO sorption-enhanced high-temperature water-gas shift (SE-WGS) reaction for hydrogen production, Appl. Energy 178 (2016) 844–855.

[15] B. Dou, C. Wang, Y. Song, H. Chen, B. Jiang, M. Yang, Y. Xu, Solid sorbents for in-situ CO_2 removal during sorption-enhanced steam reforming process: A review, Renew. Sust. Energy Rev. 53 (2016) 536–546.

[16] J. Chen, L. Duan, Z. Sun, Review on the development of sorbents for calcium looping, Energy Fuel 34 (2020) 7806–7836.

[17] Y. Wang, M.Z. Memon, M.A. Seelro, W. Fu, Y. Gao, Y. Dong, G. Ji, A review of CO_2 sorbents for promoting hydrogen production in the sorption-enhanced steam reforming process, Int J. Hydrog. Energy 46 (2021) 23358–23379.

[18] R.W. Stevens, A. Shamsi, S. Carpenter, R. Siriwardane, Sorption-enhanced water gas shift reaction by sodium-promoted calcium oxides, Fuel 89 (2010) 1280–1286.

[19] S.M. Kim, A. Armutlulu, A.M. Kierzkowska, D. Hosseini, F. Donat, C.R. Müller, Development of an effective bi-functional Ni-CaO catalyst-sorbent for the sorption-enhanced water gas shift reaction through structural optimization and the controlled deposition of a stabilizer by atomic layer deposition, Sustain Energy Fuels 4 (2020) 713–729.

[20] U. Suwanmanee, D. Saebea, V. Hacker, S. Assabumrungrat, A. Arpornwichanop, S. Authayanun, Conceptual design and life cycle assessment of decentralized power generation by HT-PEMFC system with sorption enhanced water gas shift loop, Energy Convers. Manag. 171 (2018) 20–30.

[21] C. Han, D.P. Harrison, Simultaneous shift reaction and carbon dioxide separation for the direct production of hydrogen, Chem. Eng. Sci. 49 (1994) 5875–5883.

[22] S. Ramkumar, L. Fan, Calcium looping process (CLP) for enhanced noncatalytic hydrogen production with integrated carbon dioxide capture, Energy Fuel. 24 (2010) 4408–4418.

[23] W. Gao, T. Zhou, Y. Gao, Q. Wang, Enhanced water gas shift processes for carbon dioxide capture and hydrogen production, Appl. Energy 254 (2019), 113700.

[24] J. Blamey, E.J. Anthony, J. Wang, P.S. Fennell, The calcium looping cycle for large-scale CO_2 capture, Prog. Energy Combust. 36 (2010) 260–279.

[25] Y. Hu, H. Lu, W. Liu, Y. Yang, H. Li, Incorporation of CaO into inert supports for enhanced CO_2 capture: A review, Chem. Eng. J. 396 (2020), 125253.

[26] C.R. Müller, R. Pacciani, C.D. Bohn, S.A. Scott, J.S. Dennis, Investigation of the enhanced water gas shift reaction using natural and synthetic sorbents for the capture of CO_2, Ind. Eng. Chem. Res 48 (2009) 10284–10291.

[27] J. Sun, Y. Yang, Y. Guo, C. Zhao, J. Zhang, W. Liu, P. Lu, Stabilized performance of Al-decorated and Al/Mg co-decorated spray-dried CaO-based CO_2 sorbents, Chem. Eng. Technol. 42 (2019) 1283–1292.

[28] J. Sun, Y. Guo, Y. Yang, W. Li, Y. Zhou, J. Zhang, W. Liu, C. Zhao, Mode investigation of CO_2 sorption enhancement for titanium dioxide-decorated CaO-based pellets, Fuel 256 (2019), 116009.

[29] A.H. Soleimanisalim, M.H. Sedghkerdar, D. Karami, N. Mahinpey, Pelletizing and coating of synthetic zirconia stabilized calcium based sorbents for application in calcium looping CO_2 capture, Ind. Eng. Chem. Res 56 (2017) 5395–5402.

[30] M. Zhang, Y. Peng, Y. Sun, P. Li, J. Yu, Preparation of CaO-Al_2O_3 sorbent and CO_2 capture performance at high temperature, Fuel 111 (2013) 636–642.

[31] X. Ma, Y. Li, C. Chi, W. Zhang, J. Shi, L. Duan, CO_2 capture performance of mesoporous synthetic sorbent fabricated using carbide slag under realistic calcium looping conditions, Energy Fuel 31 (2017) 7299–7308.

[32] M.S. Yancheshmeh, H.R. Radfarnia, M.C. Iliuta, Sustainable production of high-purity hydrogen by sorption enhanced steam reforming of glycerol over CeO_2-promoted $Ca_9Al_6O_{18}$-CaO/NiO bifunctional material, ACS Sustain Chem. Eng. 5 (2017) 9774–9786.

[33] J. Chen, L. Duan, Z. Sun, Accurate control of cage-like CaO hollow microspheres for enhanced CO_2 capture in calcium looping via a template-assisted synthesis approach, Environ. Sci. Technol. 53 (2019) 2249–2259.

[34] X. Ma, Y. Li, X. Huang, T. Feng, M. Mu, Sorption-enhanced reaction process using advanced Ca-based sorbents for low-carbon hydrogen production, Process Saf. Environ. 155 (2021) 325–342.

[35] C. Dang, W. Yang, J. Zhou, W. Cai, Porous Ni-Ca-Al-O bi-functional catalyst derived from layered double hydroxide intercalated with citrate anion for sorption-enhanced steam reforming of glycerol, Appl. Catal. B-Environ. 298 (2021), 120547.

[36] F. Liu, W. Li, B. Liu, R. Li, Synthesis, characterization, and high temperature CO_2 capture of new CaO based hollow sphere sorbents, J. Mater. Chem. A. 1 (2013) 8037–8044.

[37] C. Huang, M. Xu, X. Huai, Z. Liu, Template-free synthesis of hollow CaO/Ca$_2$SiO$_4$ nanoparticle as a cyclically stable high-capacity CO$_2$ sorbent, ACS Sustain Chem. Eng. 9 (2021) 2171–2179.

[38] X. Ma, Y. Li, X. Yan, W. Zhang, J. Zhao, Z. Wang, Preparation of a morph-genetic CaO-based sorbent using paper fibre as a biotemplate for enhanced CO$_2$ capture, Chem. Eng. J. 361 (2019) 235–244.

[39] M. Broda, C.R. Müller, Synthesis of highly efficient, Ca-based, Al$_2$O$_3$-stabilized, carbon gel-templated CO$_2$ sorbents, Adv. Mater. 24 (2012) 3059–3064.

[40] A. Armutlulu, M.A. Naeem, H. Liu, S.M. Kim, A. Kierzkowska, A. Fedorov, C. R. Müller, Multishelled CaO microspheres stabilized by atomic layer deposition of Al$_2$O$_3$ for enhanced CO$_2$ capture performance, Adv. Mater. 29 (2017), 1702896.

[41] N.H. Florin, A.T. Harris, Reactivity of CaO derived from nano-sized CaCO$_3$ particles through multiple CO$_2$ capture-and-release cycles, Chem. Eng. Sci. 64 (2009) 187–191.

[42] J. Chen, T. Shi, L. Duan, Z. Sun, E.J. Anthony, Microemulsion-derived, nanostructured CaO/CuO composites with controllable particle grain size to enhance cyclic CO$_2$ capture performance for combined Ca/Cu looping process, Chem. Eng. J. 393 (2020), 124716.

[43] C. Dang, L. Liu, G. Yang, W. Cai, J. Long, H. Yu, Mg-promoted Ni-CaO microsphere as bi-functional catalyst for hydrogen production from sorption-enhanced steam reforming of glycerol, Chem. Eng. J. 383 (2020), 123204.

[44] C. Chi, Y. Li, W. Zhang, Z. Wang, Synthesis of a hollow microtubular Ca/Al sorbent with high CO$_2$ uptake by hard templating, Appl. Energy 251 (2019), 113382.

[45] D. Zhang, S. Liu, X. Song, Z. Xu, B. Yang, L. Chen, Y. Tan, F. Li, Preparation of calcium titanate based on the cotton template method and its simultaneous removal performance to heavy metals and organic pollutants in water, J. Adv. Oxid. Technol. 19 (2016) 9–18.

[46] H. Sun, Y. Li, X. Yan, Z. Wang, W. Liu, CaO/CaCO$_3$ thermochemical heat storage performance of CaO-based micrometre-sized tubular composite, Energy Convers. Manag. 222 (2020), 113222.

[47] W. Dietrich, P.S. Lawrence, M. Grunewald, D.W. Agar, Theoretical studies on multifunctional catalysts with integrated adsorption sites, Chem. Eng. J. 107 (2005) 103–111.

[48] K. Gao, M.S. Yancheshmeh, J. Duchesne, M.C. Iliuta, Valorization of coal fly ash as a stabilizer for the development of Ni/CaO-based bifunctional material, ACS Sustain Chem. Eng. 8 (2020) 3885–3895.

[49] M.S. Yancheshmeh, M.C. Iliuta, Embedding Ni in Ni-Al mixed-metal alkoxide for the synthesis of efficient coking resistant Ni-CaO-based catalyst-sorbent bifunctional materials for sorption-enhanced steam reforming of glycerol, ACS Sustain Chem. Eng. 8 (2020) 16746–16756.

[50] M. Kong, K.O. Albrecht, B.H. Shanks, T.D. Wheelock, Development of a combined catalyst and sorbent for the water gas shift reaction, Ind. Eng. Chem. Res 53 (2014) 9570–9577.

[51] D. Damma, P.G. Smirniotis, Recent advances in iron-based high-temperature water-gas shift catalysis for hydrogen production, Curr. Opin. Chem. Eng. 21 (2018) 103–110.

[52] S. Natesakhawat, X. Wang, L. Zhang, U.S. Ozkan, Development of chromium-free iron-based catalysts for high-temperature water-gas shift reaction, J. Mol. Catal. A-Chem. 260 (2006) 82–94.

[53] D. Damma, T. Boningari, P.G. Smirniotis, High-temperature water-gas shift over Fe/Ce/Co spinel catalysts: Study of the promotional effect of Ce and Co, Mol. Catal. 451 (2018) 20–32.

[54] L. Han, K. Ma, Y. Wu, N. Jing, L. Jin, P. Wu, G. Xu, J. Xia, C. Zhang, Promoted calcium looping H$_2$ production via catalytic reforming of polycyclic aromatic hydrocarbon using a synthesized CO$_2$ absorbent prepared by impregnation, Int J. Energy Res 45 (2021) 10409–10424.

[55] L. Di Felice, C. Courson, D. Niznansky, P.U. Foscolo, A. Kiennemann, Biomass gasification with catalytic tar reforming: A model study into activity enhancement of calcium- and magnesium-oxide-based catalytic materials by incorporation of iron, Energy Fuel 24 (2010) 4034–4045.

[56] I. Zamboni, C. Courson, A. Kiennemann, Fe-Ca interactions in Fe-based/CaO catalyst/sorbent for CO$_2$ sorption and hydrogen production from toluene steam reforming, Appl. Catal. B-Environ. 203 (2017) 154–165.

[57] D. Damma, D. Jampaiah, A. Welton, P. Boolchand, A. Arvanitis, J. Dong, P. Smirniotis, Effect of Nb modification on the structural and catalytic property of Fe/Nb/M (M = Mn, Co, Ni, and Cu) catalyst for high temperature water-gas shift reaction, Catal. Today 355 (2020) 921–931.

[58] L.Y. Dolgykh, I.L. Stolyarchuk, L.A. Staraya, I.V. Vasylenko, Y.I. Pyatnitsky, P. E. Strizhak, Steam reforming of ethanol over manganese and iron oxides for hydrogen production, Adsorpt. Sci. Technol. 33 (2015) 715–721.

[59] Y.M. Park, J.M. Cho, G.Y. Han, J.W. Bae, Roles of highly ordered mesoporous structures of Fe-Ni bimetal oxides for an enhanced high-temperature water-gas shift reaction activity, Catal. Sci. Technol. 11 (2021) 3251–3260.

[60] Y. Da, Y. Xuan, L. Teng, K. Zhang, X. Liu, Y. Ding, Calcium-based composites for direct solar-thermal conversion and thermochemical energy storage, Chem. Eng. J. 382 (2020), 122815.

[61] E. Smit, B.M. Weckhuysen, The renaissance of iron-based Fischer-Tropsch synthesis: on the multifaceted catalyst deactivation behaviour, Chem. Soc. Rev. 37 (2008) 2758–2781.

[62] H. Guo, X. Wang, H. Wang, W. Cui, M. Li, W. Xie, Double-exchange-induced effective increased CO$_2$ capture of CaO by doping bimetallic oxides with variable valence state, Chem. Eng. J. 433 (2022), 134490.

[63] Y. Fang, Y. Wang, F. Wang, C. Shu, J. Zhu, W. Wu, Fe-Mn bimetallic oxides-catalyzed oxygen reduction reaction in alkaline direct methanol fuel cells, RSC Adv. 8 (2018) 8678–8687.

[64] E. Beyreuther, S. Grafstrom, L.M. Eng, C. Thiele, K. Dorr, XPS investigation of Mn valence in lanthanum manganite thin films under variation of oxygen content, Phys. Rev. B 73 (2006), 155425.

[65] Z. Sun, X. Zhang, H. Li, T. Liu, S. Sang, S. Chen, L. Duan, L. Zeng, W. Xiang, J. Gong, Chemical looping oxidative steam reforming of methanol: A new pathway for auto-thermal conversion, Appl. Catal. B-Environ. 269 (2020), 118758.

[66] L. Cui, D. Zhao, Y. Yang, Y. Wang, X. Zhang, Synthesis of highly efficient α-Fe$_2$O$_3$ catalysts for CO oxidation derived from MIL-100(Fe), J. Solid State Chem. 247 (2017) 168–172.

[67] H. Guo, X. Kou, Y. Zhao, S. Wang, X. Ma, Role of microstructure, electron transfer, and coordination state in the CO$_2$ capture of calcium-based sorbent by doping (Zr-Mn), Chem. Eng. J. 336 (2018) 376–385.

[68] Y. Wang, J. Cui, L. Luo, J. Zhang, Y. Wang, Y. Qin, Y. Zhang, X. Shu, J. Lv, Y. Wu, One-pot synthesis of NiO/Mn$_2$O$_3$ nanoflake arrays and their application in electrochemical biosensing, Appl. Surf. Sci. 423 (2017) 1182–1187.

[69] Y. Li, Y. Li, L. Yu, Q. Hu, Q. Wang, K. Maliutina, L. Fan, Achieving excellent and durable CO$_2$ electrolysis performance on a dual-phase fuel electrode in solid oxide electrolysis cells, J. Power Sources 491 (2021), 229599.

[70] H. Guo, X. Kou, Y. Zhao, S. Wang, Q. Sun, X. Ma, Effect of synergistic interaction between Ce and Mn on the CO$_2$ capture of calcium-based sorbent: Textural properties, electron donation, and oxygen vacancy, Chem. Eng. J. 334 (2018) 237–246.

[71] X. Ma, Y. Li, C. Zhang, Z. Wang, Development of Mn/Mg-copromoted carbide slag for efficient CO$_2$ capture under realistic calcium looping conditions, Process Saf. Environ. 141 (2020) 380–389.

[72] D. Li, H. Xue, R. Hu, Effect of Ce/Ca ratio in Ni/CeO$_2$-ZrO$_2$-CaO catalysts on high-purity hydrogen production by sorption-enhanced steam reforming of acetic acid and bio-oil, Ind. Eng. Chem. Res 59 (2020) 1446–1456.

[73] R. Koirala, K.R. Gunugunuri, S.E. Pratsinis, P.G. Smirniotis, Effect of zirconia doping on the structure and stability of CaO-based sorbents for CO$_2$ capture during extended operating cycles, J. Phys. Chem. C 115 (2011) 24804–24812.

[74] J.Y. Lee, D. Lee, K. Lee, Y. Wang, Cr-free Fe-based metal oxide catalysts for high temperature water gas shift reaction of fuel processor using LPG, Catal. Today 146 (2009) 260–264.

[75] G. Wang, Y. Guo, J. Yu, F. Liu, J. Sun, X. Wang, T. Wang, C. Zhao, Ni-CaO dual function materials prepared by different synthetic modes for integrated CO$_2$ capture and conversion, Chem. Eng. J. 428 (2022), 132110.

[76] J. Kong, Z. Xiang, G. Li, T. An, Introduce oxygen vacancies into CeO$_2$ catalyst for enhanced coke resistance during photothermcatalytic oxidation of typical VOCs, Appl. Catal. B-Environ. 269 (2020), 118755.

[77] Y. Yi, H. Liu, B. Chu, Z. Qin, L. Dong, H. He, C. Tang, M. Fan, L. Bin, Catalytic removal NO by CO over LaNi$_{0.5}$M$_{0.5}$O$_3$ (M=Co, Mn, Cu) perovskite oxide catalysts: Tune surface chemical composition to improve N$_2$ selectivity, Chem. Eng. J. 369 (2019) 511–521.

[78] J. Ling, Y. Dong, P. Cao, Y. Wang, Y. Li, Preparation of Mn-Fe oxide by a hydrolysis-driven redox method and its application in formaldehyde oxidation, ACS Omega 6 (2021) 23274–23280.

[79] M. Okumura, J.M. Coronado, J. Soria, M. Haruta, J.C. Conesa, EPR study of CO and O$_2$ interaction with supported Au catalysts, J. Catal. 203 (2001) 168–174.

[80] X. Yu, L. Dai, J. Deng, Y. Liu, L. Jing, X. Zhang, R. Gao, Z. Hou, L. Wei, H. Dai, An isotopic strategy to investigate the role of water vapor in the oxidation of 1,2-dichloroethane over the Ru/WO$_3$ or Ru/TiO$_2$ catalyst, Appl. Catal. B-Environ. 305 (2022), 121037.